POLITECNICO DI TORINO

Corso di Laurea Magistrale
in Ingegneria Aerospaziale

Tesi di Laurea Magistrale

Multiple-input active aeroelastic control using the receptance method on a flexible wing

Relatori
prof. Alfonso Pagani
dott. Sebastiano Fichera

Candidato
Francesco Palazzo
matricola 230849

A.A.2017-2018

Ai miei genitori per avermi sempre sostenuto e incoraggiato.
A tutti i parenti, amici e conoscenti per aver creduto in me.
A Gianfranca per essermi stata vicina in ogni momento.

Acknowledgements

I want to express my gratitude to the people who helped me to develop this thesis.

First of all, I thank profusely my advisor, dott. Sebastiano Fichera, for the great opportunity he offered me. I took part to this project that allowed me to learn a lot of things about control activity. His guidance was really important, because he provided me precious information, useful to do the best. Step by step he supervised me, and I reached a significant result thanks to his support.

I am extremely grateful to dott. Bilal Mokrani, who worked with me in this project and explained me everything regarding feedback control, and not just. We shared every problems happened on the experimental wing, helping each other to fix them. He imparted me his expertise and knowledge, which will help me in the future.

Many thanks to dott. Liam Adamson, for his contribution in my thesis and his friendship during the time spent in the University of Liverpool. My gratitude goes also to all the other colleagues and friends in Liverpool.

And last but not least, it is my privilege to express my sense of appreciation to my supervisor, prof. Alfonso Pagani, for accepting his role. I thank him for his good words and his pride on my work. I reached the end without preoccupations also because of his support.

Abstract

Recent trends in aircraft design show a growing interest in lightweight materials and non-conventional configurations, with the problem of increasing the frequency of occurrence of aeroelastic phenomena. Hence, active control methods become necessary to avoid aeroelastic instabilities, in particular for flutter suppression. The so called *Receptance Method* is an active control approach that shifts some of the poles of a system to new desired positions, while retaining the others unchanged. This method is useful for increasing the flutter boundary, by moving that poles whose interaction leads to the instability. Experimental implementation of the receptance method was performed on the MODular aeroelastic FLEXible wing (MODFLEX), with a Multiple-Input Multiple-Output (MIMO) control strategy. The method was so proved, with an increase of flutter speed up to 22%. Furthermore, a numerical model of the wing was developed and validated with some tests.

Sommario

Le recenti tendenze nella progettazione di velivoli mostrano un interesse crescente verso i materiali ultraleggeri e le configurazioni non convenzionali, causando però una più frequente insorgenza dei fenomeni aeroelastici. I metodi di controllo attivo diventano così necessari per evitare le instabilità che comportano, ed in particolare per evitare il fenomeno del flutter. Il *Metodo delle Recettanze* è un tipo di controllo attivo che permette di spostare alcuni poli di un sistema posizionandoli dove si desideri, senza influire sugli altri poli. Così facendo, è possibile incrementare la velocità di flutter muovendo quei poli la cui interazione provoca l'instabilità. Un'applicazione sperimentalmente del metodo delle recettanze è stata effettuata sull'ala aeroelastica, flessibile e modulare chiamata MODFLEX, utilizzando una strategia di controllo con input e output multipli. Il metodo è stato così dimostrato, ottenendo un aumento della velocità di flutter fino al 22%. Inoltre, è stato anche sviluppato un modello numerico dell'ala, validato tramite alcuni test.

Contents

List of Figures

List of Tables

Chapter 1

Introduction

To improve flight performance while at the same time reducing operating costs, recent aircraft designs employ lightweight structures, thanks to new materials and manufacturing processes. Moreover, many non-conventional aircraft configurations are being considered in the last years. These innovations, however, impacted on the aircraft stability, leading to aeroelastic problems more frequently. Hence, active control methods have been investigated with more attention to avoid instabilities on aeroelastic systems and, sometimes, to safely exploit the benefits of aeroelastic phenomena.

This introduction contains an overview on the field of aeroelasticity, with an historical background, and focuses in particular the flutter phenomenon. Then, active aeroelastic control methods are presented.

1.1 Aeroelasticity

The flight of an aircraft, rocket or space shuttle inside the Earth's atmosphere involves the contact between their structure and the airflow at high speed, which leads to an interaction between aerodynamic, elastic and inertial forces. Aeroelasticity is the branch of physics that studies phenomena generated by this interaction. A classification of the major disciplines related with the aeroelastic field of study is well represented by the Collar's triangle in Figure 1.1. It is usual to divide aeroelastic phenomena into static and dynamic, by considering whether or not to neglect inertial forces of a structure.

1.1.1 Static aeroelasticity

Static aeroelasticity considers only static aerodynamic forces (independent of time), acting on an elastic structure, while inertial forces are neglected. An important static phenomenon is *divergence*. It occurs at a certain flight speed called divergence point, in which the aerodynamic load increases the deflection of a system (usually a wing or any lifting

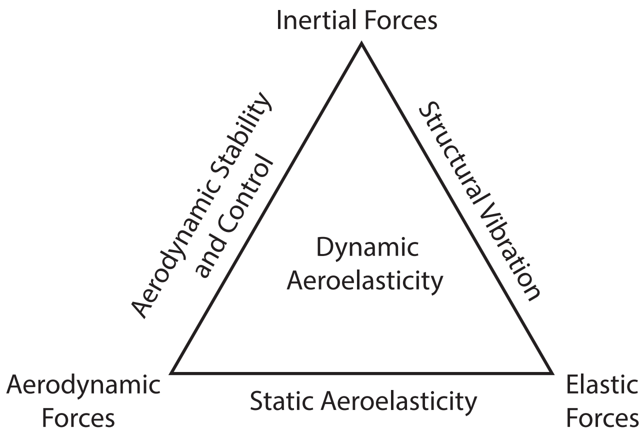

Figure 1.1: Collar's aeroelastic triangle

surface), so increasing the load on it. It is an unstable phenomenon without an equilibrium condition, so it can be really disastrous.

Another static problem is the reduction of control surfaces' effectiveness, which may result in *control reversal*. In this situation the usual functionality of control surfaces, frequently ailerons, is reversed, leading also to the aircraft fail.

1.1.2 Dynamic aeroelasticity

Dynamic aeroelasticity considers all aerodynamic, elastic and inertial forces. The main catastrophic dynamic phenomenon is *flutter*, which occurs beyond a flight speed called flutter point. In modern aircraft this point is usually reached before the divergence point, so the focus on this problem is much greater. When an aircraft approaches the flutter point, its structure (usually the wing) extracts energy from the air stream and it starts to swing with an amplitude that increases until the structure failure. This unstable self-excited oscillation is due to a coupling of system modes, which become negatively damped. Thus, it is important to predict the flutter point, but it is difficult because of the unsteady nature of aerodynamic forces and moments generated by the oscillation.

There are two types of flutter: hard flutter and soft flutter. A hard flutter occurs when the damping values drop very rapidly with a speed increase towards the flutter point, while a soft flutter is a smoother condition. Naturally, hard flutter is more dangerous because, in that case, a stable system becomes unstable with a small increment of air speed, so it is more difficult to predict the flutter point experimentally without breaking the structure.

There are different way to predict flutter, well explained by Hodges and Pierce [1]. *Classical flutter analysis* was used until the late 1970s and it was useful only to predict the flutter point, with no information about the behaviour of the system away from that point. On the other hand, the *p-method* solves the aeroelastic system equations and calculates the dimensionless parameter p, called "reduced eigenvalue", for a range of airspeed values.

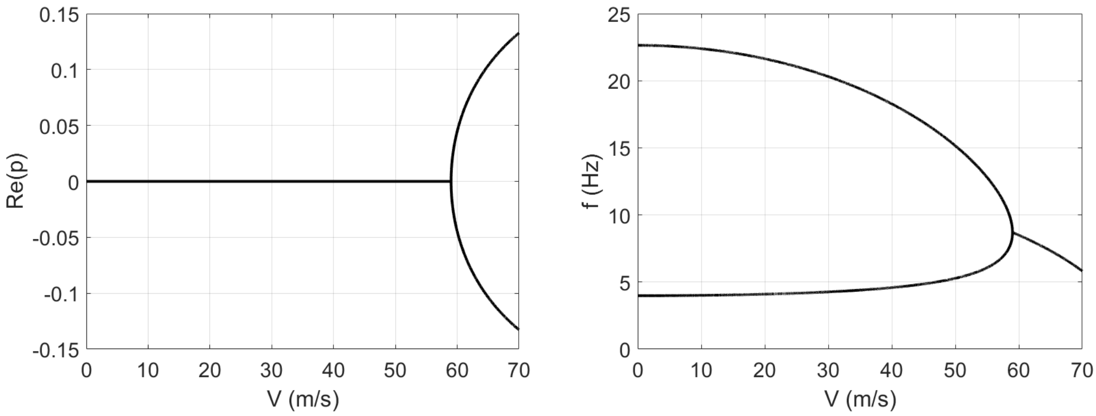

(a) **(b)**

Figure 1.2: Example of graphs obtained with the p-method: (a) real part of p and (b) natural frequencies of a wing with an airflow across it at speed between 0 and 70 m/s

Since p is related with complex eigenvalues, it is also a complex number. In Figure 1.2 there is an example of graphs obtained with the p-method applied on a wing. Only the first 2 modes are considered. In the left-hand side, the real part of p is plotted in a range of airflow velocity from 0 to 70 m/s. In the other side, the vibrational frequencies, which are directly related with the imaginary part of p, are plotted for the same range. The flutter instability occurs when the real part of p becomes positive, at about 60 m/s. At the same speed, the frequencies approach and couple, becoming a mixed mode over the flutter point.

There are other engineering solutions for flutter called k-method and p-k method. The *k-method* considers the aerodynamic damping and stiffness as functions of the "reduced frequency" k. Furthermore, a fictitious damping g is added to the system of equations, related with the damping ratio ζ by $g = -2\zeta$. The graph of g versus the airflow velocity V shows the flutter point when g becomes zero (this method is also called V-g method). Plotting also the frequencies, information about the mechanism that leads to flutter can be obtained. This method is widely used by industries for its speed of computation, but its mathematical formulation is not accurate and sometimes the results obtained away from the flutter point are not correct. The *p-k method* solves the problems of the k-method. It is a combination of the p-method and the k-method, so p is now considered as function of the reduced frequency k. As said, this method gives better results than the k-method about the prediction before and after the flutter point. Graphs obtained with the p-k method, applied on the same wing of the previous example, are in Figure 1.3. These graphs show that the real part of p becomes zero at about 55 m/s. Moreover, the frequencies do not couple together at the flutter point, but they approach each other with the air speed increase.

Flutter is not the only dynamic aeroelastic phenomenon. Other important dynamic instabilities are *Limit Cycle Oscillation* (LCO), which involves non-linear systems, and *buffeting*. However, these phenomena will not be discussed here.

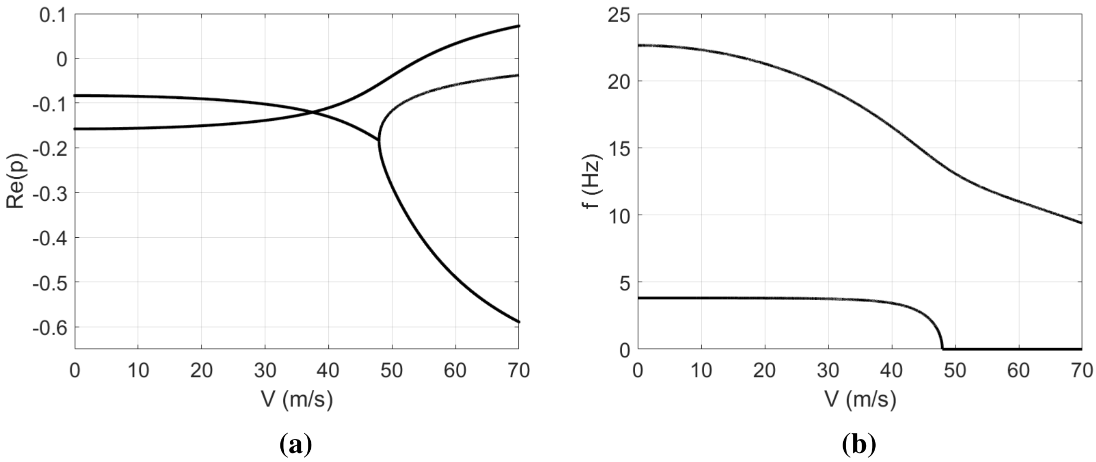

Figure 1.3: Example of graphs obtained with the p-k method: (a) real part of p and (b) natural frequencies of a wing with an airflow across it at speed between 0 and 70 m/s

1.1.3 History of aeroelasticity

Aeroelasticity is not a recent discipline and it is not only concerned with the aerospace sector, but it is also relevant in fast cars and bridge construction. Indeed, it is famous the collapse of the Tacoma Narrows Bridge in 1940 caused by flutter, occurred because of a high speed violent wind, as explained by Billah and Scanlan [2]. Anyway, the first recorded flutter phenomenon occurred to an aircraft, the Handley Page O/400 bomber in 1916, so the problem was in that moment studied and solved for the fist time by Lanchester [3] and by Bairstow and Fage [4]. They found that the failure was caused by the horizontal tail which had two elevators independently actuated. An antisymmetric elevator mode coupled with a fuselage torsional mode led to a self-excited oscillation until the failure. Other accidents linked with aeroelastic phenomena were experienced by aeroplanes during next years until nowadays. Thus, it was learned that a way to avoid them is with an aeroelastic design, so a focus on aeroelasticity during the aircraft design.

A great number of books deal with aeroelasticity. Some of them are more classical, e.g. Fung [5] (1955), Bisplinghoff et al. [6] (1955), Dowell et al. [7] (1978), while other are more recent, e.g. Hodges and Pierce [1] (2002), Wright and Cooper [8] (2007). Many of these books deal with cantilever wings and consider unsteady aerodynamic, so they give theoretical information. Instead, the aeroelastic design of an aerospace system is usually carried out with structural and aerodynamic Finite Element models in order to predict aeroelastic phenomena. Then, validation of results is done with wind tunnel tests or during flight experiments.

For several decades, research activity has been focused to reduce all negative effects of aeroelastic phenomena. In addition to aeroelastic design, different aeroelastic control methods have been developed, with the purpose to solve many catastrophic aeroelastic problems not revealed during the design process.

1.2 Aeroelastic control

Flutter is a catastrophic phenomenon that needs to be eliminated, or at least it has to occur at speeds far beyond the flight envelope. Flutter suppression could be performed with feedback control methods, increasing the flutter boundary by assigning stable poles to the system.

The problem of vibration suppression is of interest to engineers from almost one century. Two approaches may be used to solve it: a passive physical modification and an active control [9]. Passive modifications have been examined by Duncan [10] from 1941. Adding structural elements to a system such as masses, springs or patches, a number of poles and zeros can be assigned. However, also the static behaviour of the system is affected in this way. This method has a limit on the number of eigenvalues that can be changed and physical limits related with the form and dimension of additional elements. Furthermore, it is not possible to change poles during flight.

Active controls spread years later, also thanks to Wonham [11] in 1967. He showed that poles of a controllable dynamic systems can be reassigned with a state feedback. Several active control methods have been developed until nowadays, and many of them are described by Inman [12] and Fuller et al. [13]. Partial pole placement is an active control method useful to move some poles of a system to desired position, retaining the others unchanged. Datta et al. [14] first proposed the method in 1997, optimized during years to make it a robust procedure [15]. However, it needs to know the system matrices, which can be estimated only with Finite Element method for complex systems.

On the other hand, a recent control algorithm known as *receptance method*[1] was presented by Ram and Mottershead [16] in 2007. This method requires only experimental measured receptances of the system, so it does not require to know or to evaluate mass, damping and stiffness matrices. Furthermore, there is no need of model reduction methods, or to estimate the unmeasured states. The formulation was implemented in several ways and it followed some developments during years: the paper by Mottershead et al. [17] shows how the eigenvalue sensitivities can also be assigned, Ram et al. [18] describe the effect of time delay. An application on a T-shape plate is described by Mottershead et al. [19], while Tehrani et al. [20] tested the method on a lightweight composite beam and on a modular test structure. The formulation was also implemented on an Agusta-Westland W30 helicopter airframe, with a ground vibration test, in 2012 [21].

The receptance method underwent a reformulation in 2013, as described by Ram and Mottershead [22], which made it faster and more general. Indeed, the original method [16] was readily usable for a single-input control, while the multiple-input case was achievable only with a sequence of single-input applications. Furthermore, it needed the Sherman-Morrison formula [23] to determine the closed loop receptances. On the other hand, the new reformulation can be used for a multiple-input control in one step, and it

[1]The receptance is the ratio between the vibrational displacement of a structure and its exciting force.

allows to assign both eigenvalues and eigenvectors. The new reformulation is theoretically demonstrated with some examples performed on a mass-spring-damper dynamic system. The system is described by the quadratic pencil with its mass, damping and stiffness matrices, **M**, **C** and **K** respectively. The receptance matrix is obtained from the inverse of the dynamic stiffness, which is related with the previous matrices, but practically it could be measured experimentally from the system. Then, the receptance algorithm allows to determine feedback gains, **G** and **F**, which multiply displacement and velocity feedbacks of the system respectively, in order to perform the closed loop control.

An experimental application of the receptance method in its reformulated form was carried out by Fichera et al. [24], but only for the single-input control case.

1.3 Purpose of the study

The main purpose of this work is to demonstrate the experimental feasibility of the reformulated receptance method in its complete Multiple-Input Multiple-Output (MIMO) form, by applying it on a flexible wing, with two control surfaces as actuators and two laser sensors that read the vertical displacement of the wing. The second objective is to increase the flutter boundary of the wing, thanks to the shift of its poles with the receptance method: moving a pole in the s-plane means that the natural frequency and damping of the related mode also change. Indeed, in a complex system, the eigenvalue λ is related with the natural frequency ω_n and the damping value ζ by the equation

$$\lambda = \sigma + i\eta = -\omega_n\zeta \pm i\omega_n\sqrt{1-\zeta^2} \tag{1.1}$$

where σ is the real part and η is the imaginary part of the pole.

In accordance with the flutter prediction methods that are described in section 1.1.2, it is possible to increase the flutter boundary by increasing the frequency separation of its critical modes or by increasing their damping value. In this way, the flutter phenomenon may be moved at higher speeds.

The next chapter includes the flexible wing design and its disposition for a wind tunnel test. A numerical model of the wing is also described and validated by comparing it with the experimental wing. Chapter 3 explains the most recent reformulation of the receptance method and its implementation in MATLAB. Applications of the method on the numerical model and on the experimental wing are presented in the last two chapters.

Chapter 2

Aeroelastic model

The experimental wing used to implement the multiple-input receptance method is called MODFLEX wing (MODular aeroelastic FLEXible wing). It is the latest development of the experimental wing used by Fichera et al. [24] to perform the single-input control case, which now has been updated with multiple control surfaces.

This chapter presents the aeroelastic experimental and numerical models of the wing, and shows the results of a comparison between them in terms of a modal analysis and a flutter test.

2.1 Experimental model

The modular nature of the wing allows it to be used in different configurations to perform various analysis. This section contains all the information about the wing design and its disposition for the experimental analysis.

2.1.1 MODFLEX wing design

The MODFLEX wing was designed as composed by 4 modular aerodynamic sectors and a tip sector made with 3D printing technologies, while an aluminium alloy spar is the only structural element. The MODFLEX wing design is shown in Figure 2.1. Although the initial wing design was with 4 control surfaces on two sectors as in figure, the multiple-input control was performed with the only 2 control surfaces on the 4^{th} sector (TEO - Trailing Edge Outer and LEO - Leading Edge Outer), keeping as passive the 2^{nd} sector. The configuration of the wing for the MIMO control analysis is shown in Figure 2.2.

About physical specifications, each sector is made by ABS, it has a chord $c = 0.3\,\mathrm{m}$ and a symmetric aerofoil NACA 0018. Mass and flexural axes are both positioned more or less at the middle of chord, so at $0.5c$, corresponding with the main spar axis. The spar is in aluminium alloy and it has a particular cross-section shape, as shown in Figure 2.3. This shape was chosen to have the desired values of flexural, torsional and in-plane

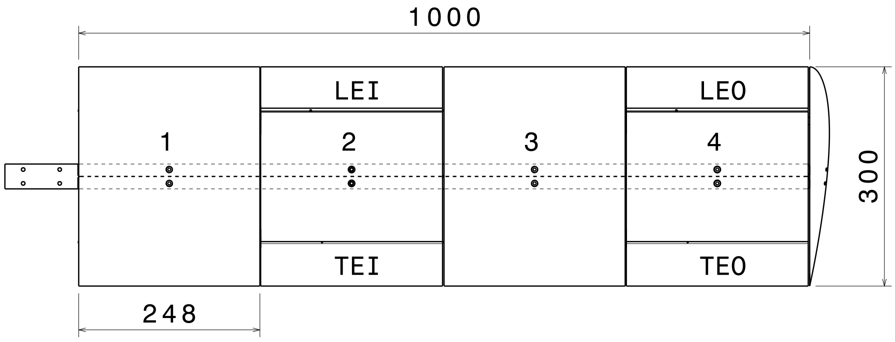

Figure 2.1: MODFLEX wing design and dimensions in millimeters

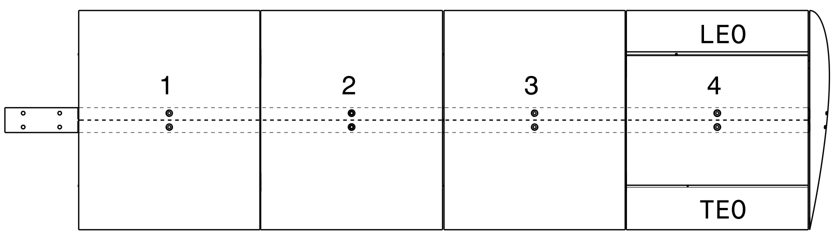

Figure 2.2: MODFLEX wing configuration with TEO and LEO control surfaces

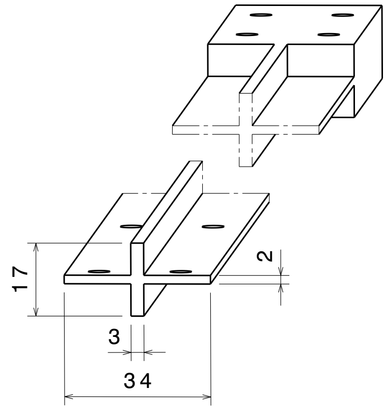

Figure 2.3: Main spar shape and dimensions in millimeters

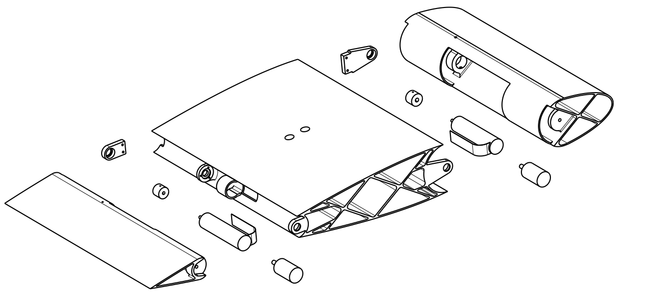

Figure 2.4: Brushless motor position for the sector with control surfaces

stiffness and to reach a certain independence between flexural and torsional ones. The main spar passes through all the sectors and it is fully constrained at one end. Each sector is connected with the main spar by 2 pins in 2 close points near the middle of chord. By setting up all sectors with some millimeters of space between them, the stiffness of the model led by the spar is not modified. Both the control surfaces are connected with the 4^{th} sector and they are actuated by motors mounted inside the connection, as shown in Figure 2.4. The control surfaces' hinge axes are at $0.2c$ and $0.8c$, while their span is the same as the sector. The chosen motors are Maxon EC 16 Ø16 mm, brushless, 60 Watt, connected with the encoders MR, Type ML, 512 CPT, 3 Channels, the planetary gearheads GP 16 C Ø16 mm, 0.2-6 Nm and the line drivers ESCON 36/3 ec, 2.7/9 A, 10-36 VDC. Specification of the motors and the gearheads are in Table 2.1. They were chosen for the high torque and the light weight.

Table 2.1: Specifications of the Maxon EC 16 Ø16 mm motor on the left, the planetary gearhead GP 16 C Ø16 mm on the right

Part number	395588
Nominal voltage	24 V
Max. continuous torque	17 mNm
Max. continuous current	3.39 A
Max. radial load	10 N
Stall torque	221 mNm
Torque constant	5.25 mNm/A
Speed constant	1820 rpm/V
Rotor inertia	1.07 gcm^2
Weight	58 g

Part number	416115
Max. continuous torque	0.5 Nm
Max. radial load	80 N
Radial play	0.08 mm
Mass inertia	0.05 gcm^2
Weight	33 g

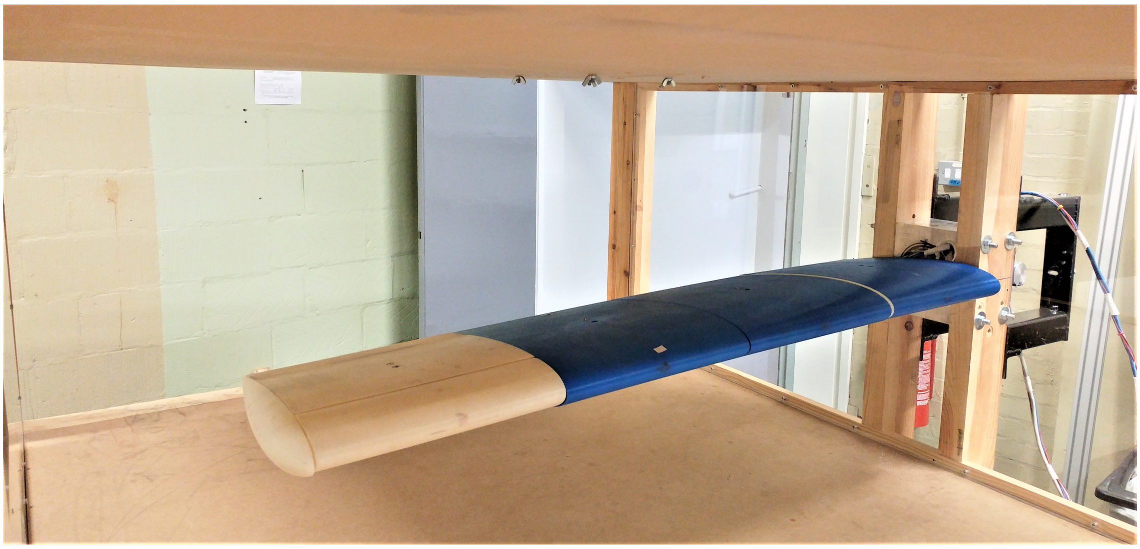

Figure 2.5: MODFLEX wing installed in the wind tunnel test section

2.1.2 MODFLEX wing disposition for MIMO control

The MODFLEX wing in the configuration shown in Figure 2.2 was fully constrained by one end with a fixing mechanism that allows to select and keep a desired angle of attack. It was chosen to keep the wing at zero degrees. The test section where the wing and the clamping are installed is a $1.2 \times 0.6 \times 1.0$ m open section. It allows a connection with the low-speed wind tunnel of the University of Liverpool, which has a maximum wind speed of 20 m/s. A photo of the wing inside the test section is shown in Figure 2.5. Whilst the system inputs are the control surfaces movement, the outputs are the displacements of two points along the chord of the 3^{rd} sector, located at $0.25c$ and $0.75c$, both at the middle of

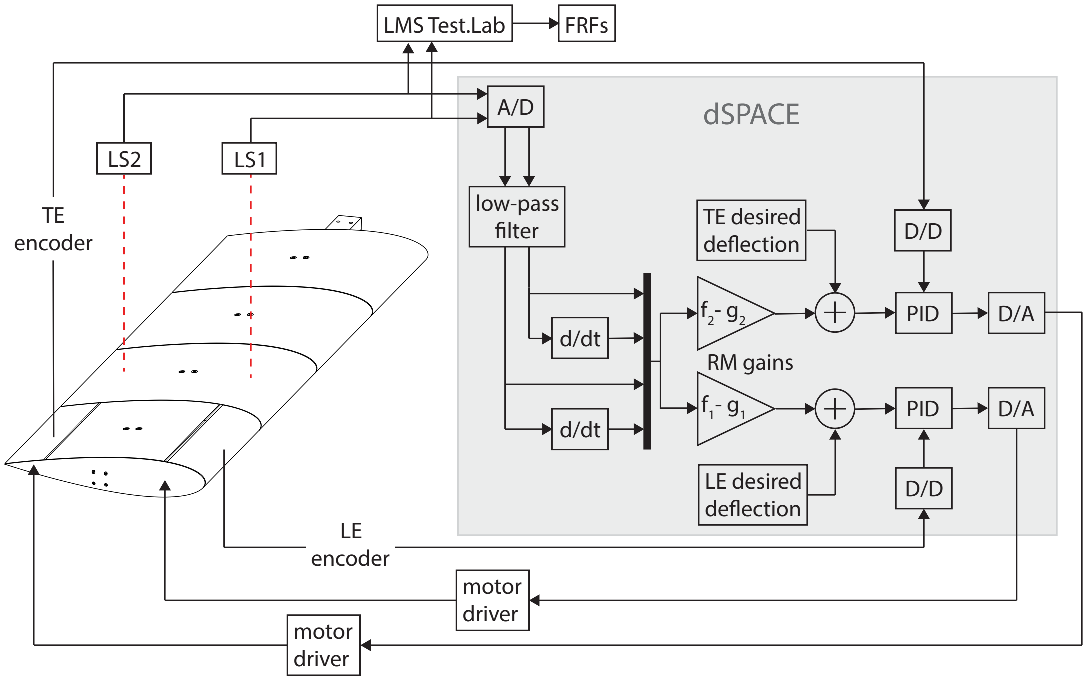

Figure 2.6: MATLAB experimental wing set-up with block diagram

its span. Two laser sensors (Keyence LK-500) mounted on the top of the test section were used for reading the above mentioned displacements.

The control algorithm was developed in MATLAB Simulink and then implemented in the real-time acquisition system dSPACE. Its purpose is to move the control surfaces as desired and to read the wing displacement with the laser sensor. In this way, Frequency Response Functions (FRFs) of the wing can be computed, necessary for the application of the receptance method. The experimental wing set-up is shown in Figure 2.6, with a block diagram to explain the control algorithm.

The wing vertical displacements are read by the laser sensors (called LS1 and LS2), whose signals pass through an Analogue to Digital converter. Then, a second-order Butterworth low-pass filter cuts off the frequencies over 10 Hz. The velocity of the wing movement is obtained by numerically deriving the displacement signals. Both displacement and velocity values are used to perform the closed loop control, multiplying them by the **F** and **G** gains obtained with the receptance method, and summing them with the desired deflection commands of the control surfaces. The readings of both the digital encoders are used as feedbacks for inner loops, which implement PID (Proportional-Integral-Derivative) controllers to ensure that the desired deflections of the control surfaces are always really reached. Furthermore, the same inner loops also allow to keep the control surfaces at zero degrees when required, so to offset their weight. This is achieved by measuring the angle values when each control surface is at its maximum and minimum

angular position. Then, the voltage linked with the middle angular value is used to keep the control surfaces at zero degrees. These inner loops produce therefore voltage outputs that pass through Digital to Analogue converters, and then go to the motor drivers, which provide current to the motors.
To summarise, the inner loops:

- use the encoder readings as feedbacks;
- implement the PID controllers;
- produce the voltage output to sent to the motor drivers, which provide current to the motors.

The outer loops:

- use the laser readings as feedbacks;
- multiply them by the gain values obtained with the receptance method;
- sum the required command with the desired deflection command and send them, through the inner loops, to the motors.

However, the outer loops are only used in a second moment, after the computation of the control gains.

The laser signals are also sent to the Siemens.PLM LMS Test.Lab acquisition system to compute 4 frequency response functions of the wing, obtained by each combination between the 2 inputs and the 2 outputs.

PID controller

A PID controller is a simple and widely used type of controller. The input to a PID is the system error, which is the difference between the system input and the feedback signal from the output. The input term, its integral and its derivative, are multiplied by gains, which correspond to the 3 terms of a PID controller: the proportional K_P, the integral K_I and the derivative K_D gains. According to Franklin et al. [25], the transfer function of PID controllers is

$$PID(s) = K_P + K_I\left(\frac{1}{s}\right) + K_D s \tag{2.1}$$

where s is the general complex eigenvalue. The proportional term gives an output proportional to the error value. The integral term eliminates the offset, which is the accumulated error over time. The derivative term improves the dynamic response of the system.

Besides a manual tuning, which needs much experience, there are various empirical methods that can be used for tuning the three gains. One commonly used is the *Ziegler–Nichols method*, introduced by J.G. Ziegler and N.B. Nichols in 1942-1943. This method can be used to set only proportional, proportional-integral or full proportional-integral-derivative controllers. The approach is to keep the integral and the derivative terms at zero and to evaluate the ultimate proportional gain K_U value. K_U is the value obtained when the system output starts to oscillate at a fixed amplitude after a step command. It is also necessary to evaluate the period of the oscillation T_U in that condition. For a complete PID controller, the three gains are obtained by

$$K_P = 0.6K_U \qquad K_I = \frac{2K_P}{T_U} \qquad K_D = \frac{K_P T_U}{8} \tag{2.2}$$

On the experimental MODFLEX wing, the feedback signal to each PID controller was sent by the encoders. Tuning with the Ziegler-Nichols method, the three gains for both the motors should be setted at

$$K_U = 2.5 \qquad T_U = 0.06 \quad \rightarrow \quad K_P = 1.5 \qquad K_I = 50 \qquad K_D = 0.0113$$

However, a manual tuning was done to adjust these values, by seeing the response of both the motors. The gain values kept were, for the LEO control surface

$$K_P = 2 \qquad K_I = 2 \qquad K_D = 0.01$$

while for the TEO control surface the gains were

$$K_P = 2 \qquad K_I = 1.5 \qquad K_D = 0.01$$

2.2 Numerical model

A numerical model of the wing was developed before the manufacturing of the experimental one. Indeed, it was used to calculate the flutter speed by varying the main spar shape, and to estimate the hinge moment for the control surfaces in order to select the proper motors.

The numerical model is composed by beam Finite Elements: 40 beam elements for the spar, 10 elements for each control surface. It has the sectors' masses concentrated in 4 points (more or less at the centre of each sector), 2% of structural damping and aerodynamic panels, which are used to solve the unsteady aerodynamic with the MD.Nastran DLM (Doublet Lattice Method). The 4 control surfaces are all implemented in the model, so they can be properly locked or unlocked when necessary. A static analysis was performed with MD.Nastran SOL101, which gave a tip vertical displacement of 39 mm due only to the wing's weight.

2.3 Comparison of numerical and experimental models

The main comparisons carried out between the numerical and the experimental models are about a modal analysis and a flutter test.

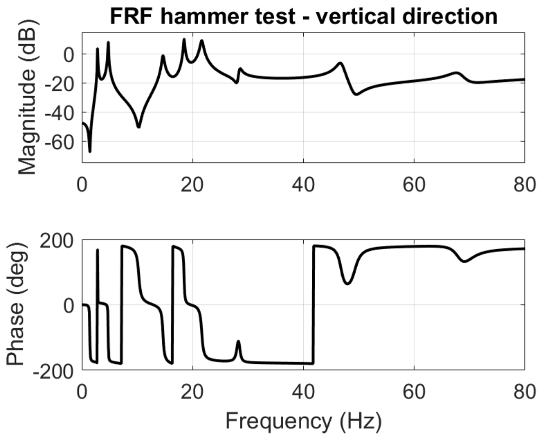

(a) impact along vertical direction

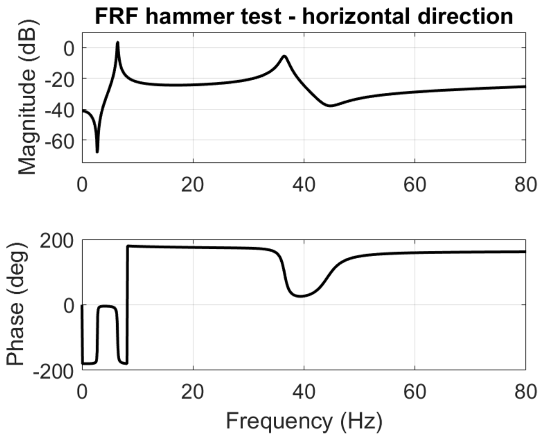

(b) impact along horizontal direction

Figure 2.7: Frequency response functions obtained with an hammer test, by impacting along different directions

2.3.1 Modal test comparison

A modal test [26] was performed on the experimental MODFLEX wing. The natural frequencies and damping were obtained by using the impact hammer technique with a web of accelerometers, and by analysing the results on the Siemens.PLM LMS Test.Lab acquisition system. In detail, both the control surfaces were fixed at zero degrees. Then, 8 accelerometers were positioned on the top of the wing, 1 near the leading edge and 1 near the trailing edge of each sector, in the middle of their span. The wing was excited by an impulsive force obtained by impacting with the hammer in a point aligned to one accelerometer, but from the wing bottom. A frequency response function was then obtained in a range from 0.1 to 80 Hz. Natural frequencies and damping values were computed from the FRF by the modal parameter estimation technique PolyMAX, described by Peeters et al. [27]. The in-plane modes are determined by placing only 4 accelerometers on the leading edge of all the sectors, and by impacting along the horizontal plane near one accelerometer. Synthesized curves of both the FRFs are in Figure 2.7.

In Table 2.2 there are the experimental results compared with those of the numerical model, obtained with MD.Nastran SOL103. This solution sequence ignores all damping, so for the numerical model only the frequencies are displayed. The error between the frequencies of the two models is also calculated.

The 10^{th} mode is different because a local mode was found numerically, while the 10^{th} experimental peak corresponded to a bending mode. Anyway, there is a small error in frequency for all the other modes, except for the 3^{rd} bending, which has almost 10 Hz of difference. This means that the numerical model is representative of the real wing for low vibrational frequencies, but an improvement is needed to fit also high frequency modes. Mode shapes are now displayed.

Table 2.2: Comparison of frequencies and damping of the numerical and experimental wing models

Mode	Mode shape	Numerical model Frequency [Hz]	Experimental model Freq. [Hz]	Experimental model Damp. ζ [%]	Error [%]
1	1^{st} bending mode	3.03	2.90	0.24	4.5
2	1^{st} torsional mode	4.97	4.81	0.65	3.3
3	1^{st} in-plane mode	6.97	6.41	1.14	8.7
4	2^{nd} torsional mode	15.07	14.64	1.22	2.9
5	2^{nd} bending mode	17.26	18.44	0.51	6.4
6	3^{rd} torsional mode	22.22	21.63	1.10	2.7
7	4^{th} torsional mode	28.21	28.42	0.98	0.7
8	3^{rd} bending mode	37.91	46.73	1.36	18.9
9	2^{nd} in-plane mode	42.05	36.47	1.80	15.3
10_N	local mode	60.29	-	-	-
10_X	4^{th} bending mode	-	67.94	2.06	-

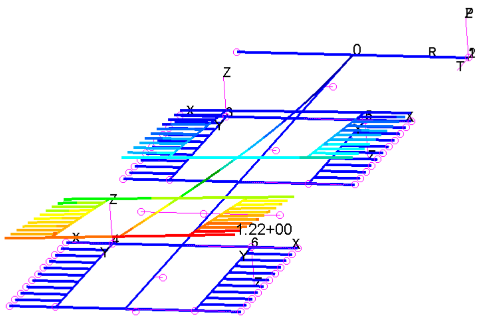

(a) 1 - 1^{st} bending mode

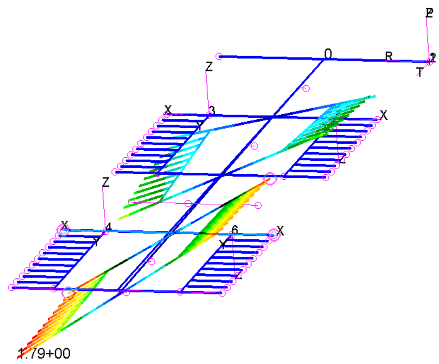

(b) 2 - 1^{st} torsional mode

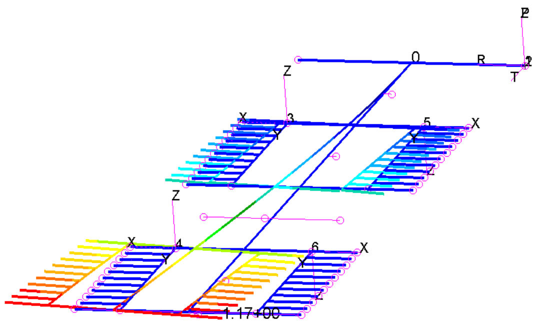

(c) 3 - 1^{st} in-plane mode

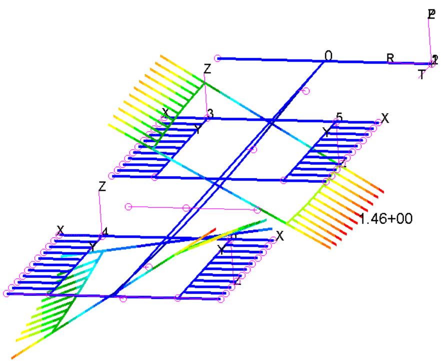

(d) 4 - 2^{nd} torsional mode

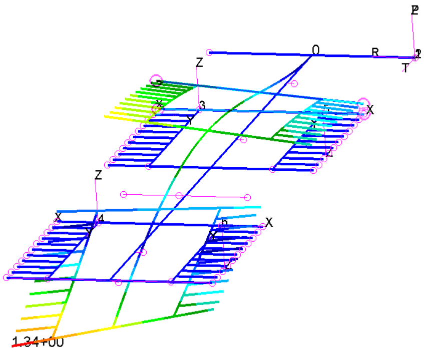

(e) 5 - 2^{nd} bending mode

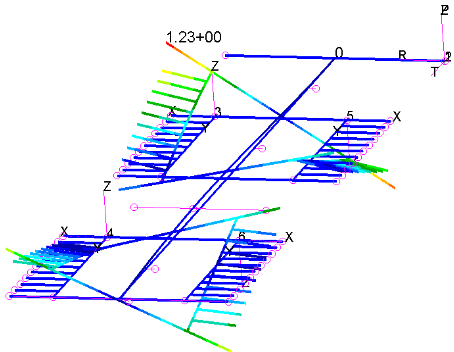

(f) 6 - 3^{rd} torsional mode

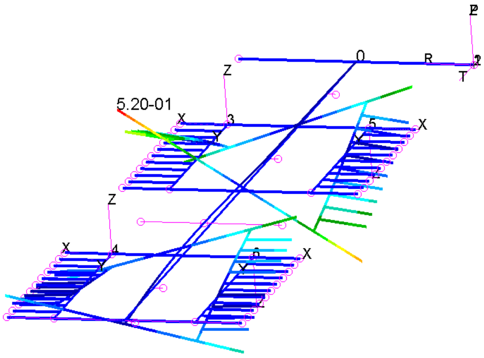

(g) 7 - 4^{th} torsional mode

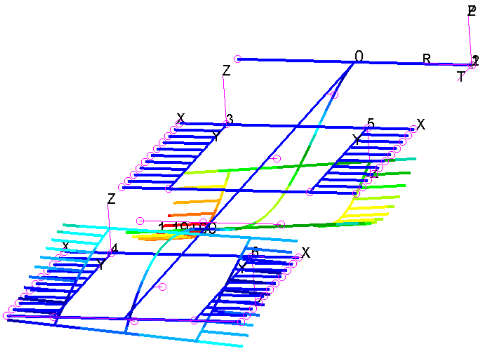

(h) 8 - 3^{rd} bending mode

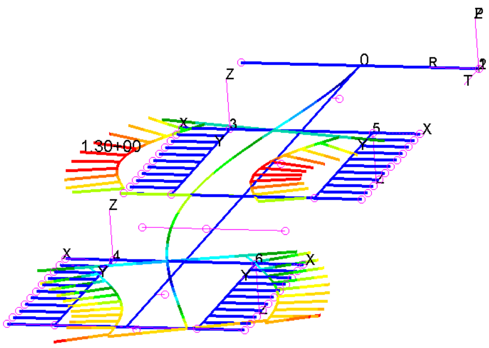

(i) 9 - 2^{nd} in-plane mode

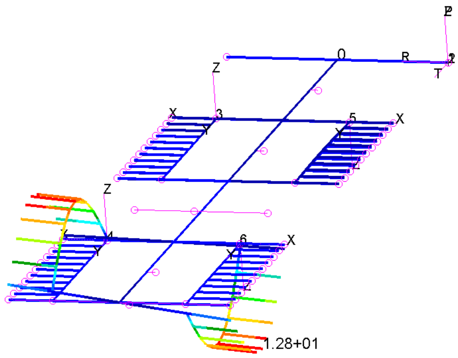

(j) 10_N - local mode

Figure 2.8: First 10 mode shapes of the wing numerical model

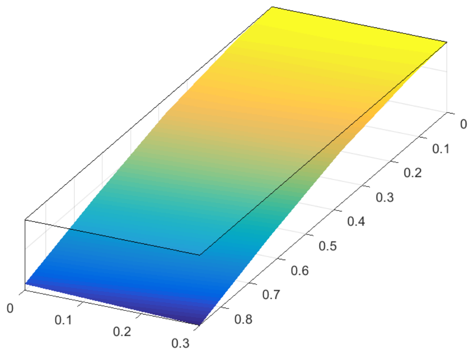

(a) 1 - 1^{st} bending mode

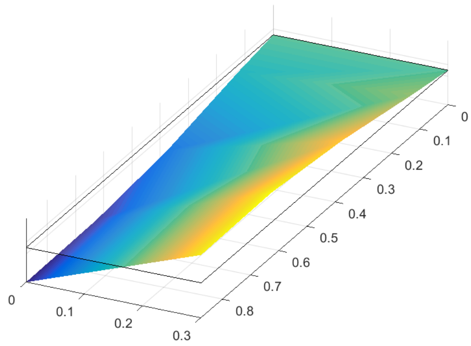

(b) 2 - 1^{st} torsional mode

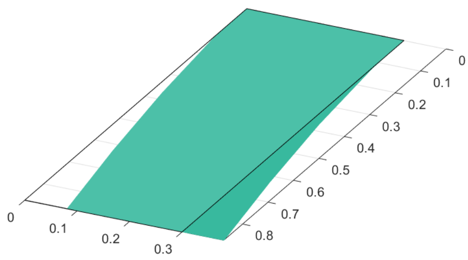

(c) 3 - 1^{st} in-plane mode

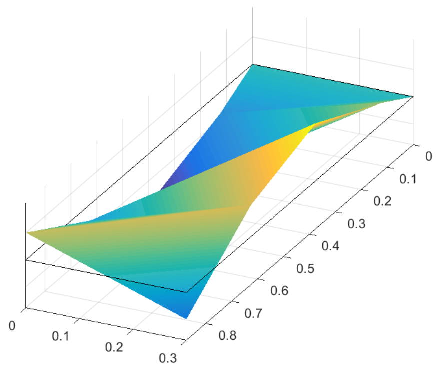

(d) 4 - 2^{nd} torsional mode

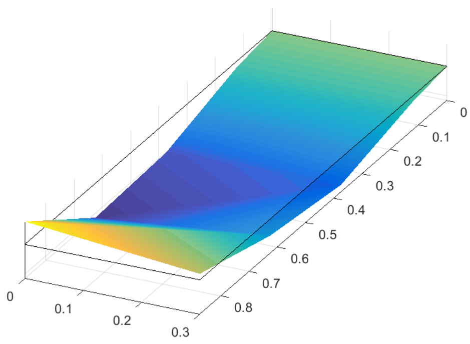

(e) 5 - 2^{nd} bending mode

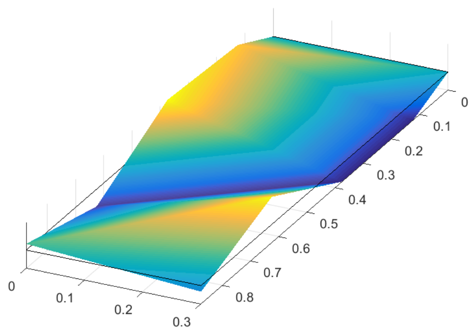

(f) 6 - 3^{rd} torsional mode

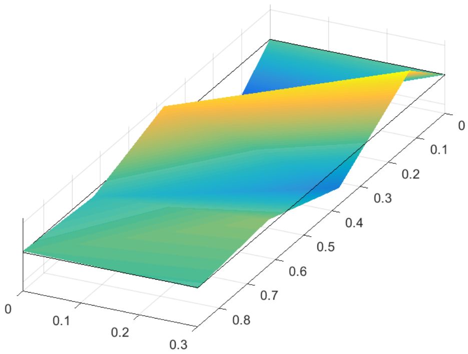

(g) 7 - 4^{th} torsional mode

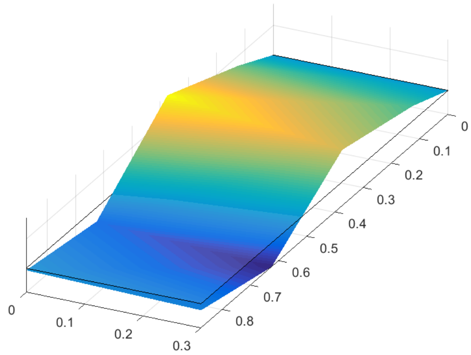

(h) 8 - 3^{rd} bending mode

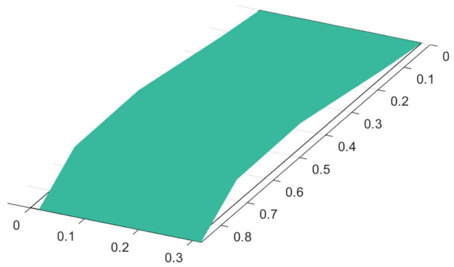

(i) 9 - 2^{nd} in-plane mode

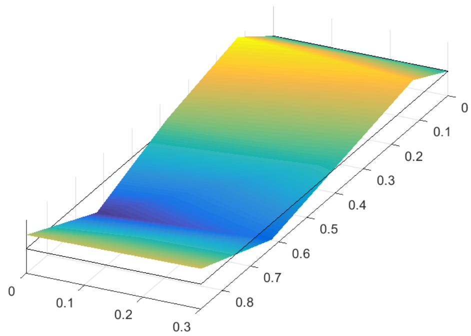

(j) 10_X - 4^{th} bending mode

Figure 2.9: First 10 mode shapes of the wing experimental model. They are computed with accelerometers positioned at 0.125 m, 0.375 m, 0.625 m and 0.875 m from the wing root

Mode shapes of the numerical wing model were obtained with the Patran post-processor and they are presented in Figure 2.8, while the experimental mode shapes were computer by LMS Test.Lab, thanks to the accelerometers disposition on the wing. In Figure 2.9, experimental modes are shown.

MAC

The so called Modal Assurance Criterion (MAC) (or also Mode Shape Correlation Criterion) quantifies the similarity between the predicted mode shapes, which are obtained by the numerical wing model, and the measured mode shapes obtained by the experimental

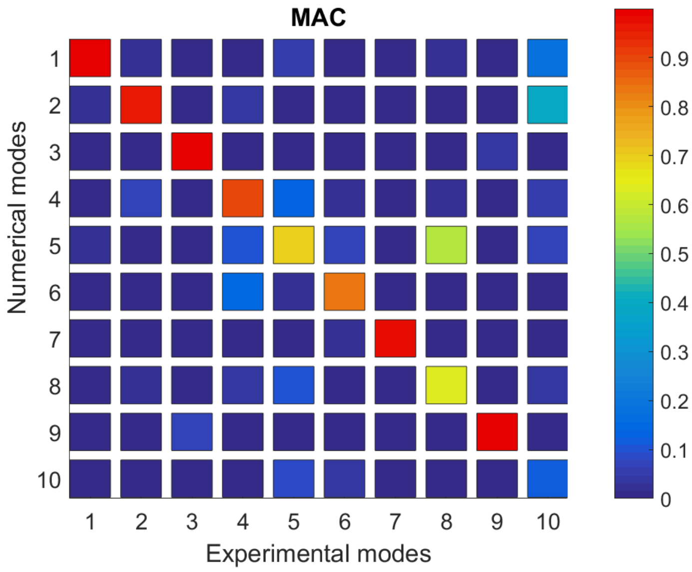

Figure 2.10: Modal Assurance Criterion for the first 10 mode shapes obtained by the numerical and the experimental model

wing. It can be also used for other comparisons, not of interest to us. This parameter is defined by the least square deviation between the numerical mode shape vector (eigenvector) φ_N and the experimental measured one φ_X, so

$$MAC(r,q) = \frac{\left|\{\varphi_N\}_r^T\{\varphi_X\}_q\right|^2}{\left(\{\varphi_N\}_r^T\{\varphi_N\}_r\right)\left(\{\varphi_X\}_q^T\{\varphi_X\}_q\right)} \qquad r = 1,\ldots,n \qquad q = 1,\ldots,m \quad (2.3)$$

where n and m are the number of analysed modes respectively from the numerical and the experimental models. The $MAC(r,q)$ parameter is a scalar quantity between 0 and 1, which indicates if the mode shapes have some correlation. A value close to 0 means that there is no correlation, so the related modes are different, while a value close to 1 means that they are the same mode. All parameters obtained with a set of numerical modes and a set of experimental modes can be presented in a matrix, which ideally is composed by values of 1 in the diagonal and 0 in the other positions.

The numerical and the experimental mode shapes shown in Table 2.2 are compared by using the MAC, and the resultant matrix is shown in Figure 2.10. As expected, there is a correlation between the first 9 modes, while the last one is different. However, some modes have not a very high MAC index, as for the 8^{th} experimental mode which has only a correlation of 0.64 with the 8^{th} numerical mode, but it has also a correlation of 0.58 with the 5^{th} numerical mode. This could mean that the numerical model needs some improvement to better fit the experimental one for high frequency modes, as also highlighted previously. However, the first 2 modes, which correspond to the 1^{st} bending

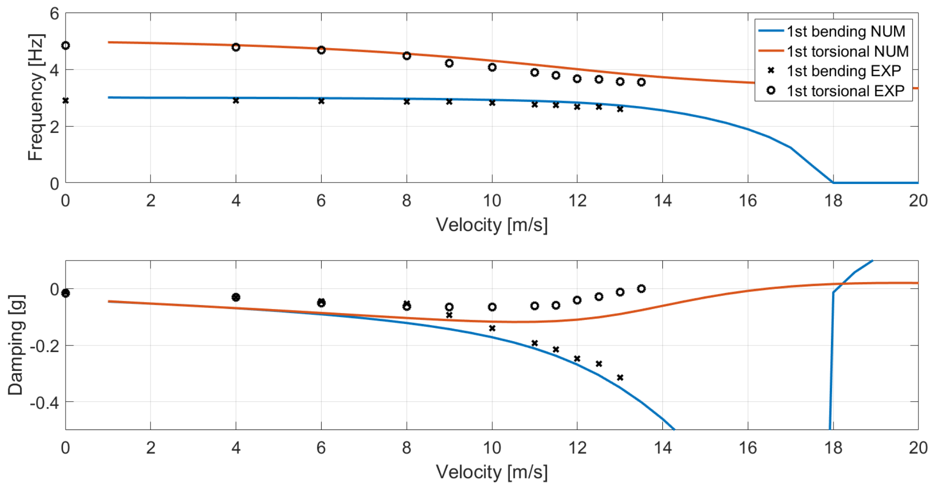

Figure 2.11: Velocity-frequency and Velocity-damping diagrams of the MODFLEX wing

and the 1^{st} torsional modes, have a correlation value near to 1, so the numerical model is enough accurate for a flutter comparison.

2.3.2 Flutter test comparison

A flutter test comparison was performed with the V-f and V-g diagrams (Velocity - frequency and Velocity - damping), by computing the 1^{st} bending and the 1^{st} torsional modes at different air speeds. For the numerical model these diagrams were computed with MD.Nastran SOL145. For the experimental wing, all the frequency and damping values were obtained by an hammer test, with the wing mounted inside the wind tunnel and the control surfaces kept fixed at zero degrees by the motors. The wind was increased, first with large steps, while near the flutter point it was increased by 0.5 m/s. However, a stepped sine excitation was used for determining some points, also at high wind speed, as comparison with the hammer test results. It gave the same frequency and damping values, so the hammer did not affect aerodynamic during the test. In Figure 2.11 the numerical results are presented in solid lines and the experimental ones with markers. Numerically, it results a flutter velocity of $V_{num} = 16\,\mathrm{m/s}$, while experimentally the flutter instability occurs with a wind speed of $V_{exp} = 13.5\,\mathrm{m/s}$. The lower flutter speed for the experimental model is also depicted by the smaller values of damping obtained, as shown in figure. The numerical model can be improved by reducing the damping values in order to fit the experimental values. In this way, the numerical flutter speed should be similar to the experimental one.

Chapter 3

Active aeroelastic control

The new reformulation of receptance method is explained in this chapter, including also an example of application on a system with 2 Degrees of Freedom, controlled by 2 inputs. The method is implemented in MATLAB by using the state-space model, and it is tested and proved with the same examples. Other tests are done on the numerical model of the wing, as shown in chapter 4.

3.1 Receptance method

The receptance method algorithm [22] is here described. The objective is to find **F** and **G** feedback gain matrices in order to perform a closed loop control, by moving some system poles to required positions.

3.1.1 MIMO receptance method

Consider a multiple-input multiple-output control system with m inputs. Let $\mathbf{M}$, $\mathbf{C}$ and $\mathbf{K} \in \mathbb{R}^{n \times n}$ be symmetric mass, damping and stiffness matrices where n is the number of Degrees of Freedom (DoFs) of the system. The quadratic eigenvalue problem associated with the open loop system is

$$(\lambda_k^2 \mathbf{M} + \lambda_k \mathbf{C} + \mathbf{K})\mathbf{v}_k = 0 \qquad k = 1, \ldots, 2n \tag{3.1}$$

where λ_k are the eigenvalues and $\mathbf{v}_k$ are the eigenvectors of the open loop system. The same problem associated now with the closed loop system is

$$(\mu_k^2 \mathbf{M} + \mu_k \mathbf{C} + \mathbf{K})\mathbf{w}_k = \mathbf{B}(\mu_k \mathbf{F}^T + \mathbf{G}^T)\mathbf{w}_k \qquad k = 1, \ldots, 2n \tag{3.2}$$

where μ_k are the eigenvalues and $\mathbf{w}_k$ are the eigenvectors of the closed loop system, $\mathbf{B} = [\mathbf{b}_1 \quad \cdots \quad \mathbf{b}_m]$ is the control force distribution matrix whose columns are the control vectors of each input, $\mathbf{F} = [\mathbf{f}_1 \quad \cdots \quad \mathbf{f}_m]$ and $\mathbf{G} = [\mathbf{g}_1 \quad \cdots \quad \mathbf{g}_m]$ are the gain matrices of the control feedback, each column for each input too. Therefore, equations (3.2) become

$$(\mu_k^2\mathbf{M}+\mu_k\mathbf{C}+\mathbf{K})\mathbf{w}_k = \big(\mathbf{b}_1(\mu_k\mathbf{f}_1^T+\mathbf{g}_1^T)+\ldots+\mathbf{b}_m(\mu_k\mathbf{f}_m^T+\mathbf{g}_m^T)\big)\mathbf{w}_k \qquad k = 1,\ldots,2n \tag{3.3}$$

Assume that the first p eigenvalues of the closed loop $\{\mu_k\}_{k=1}^{p}$ are different from those of the open loop $\{\lambda_k\}_{k=1}^{2n}$, while the others are keeping as the same, so $\mu_k = \lambda_k$ for $k = p+1,\ldots,2n$. A substitution in (3.3) gives

$$(\lambda_k^2\mathbf{M}+\lambda_k\mathbf{C}+\mathbf{K})\mathbf{w}_k = \big(\mathbf{b}_1(\lambda_k\mathbf{f}_1^T+\mathbf{g}_1^T)+\ldots+\mathbf{b}_m(\lambda_k\mathbf{f}_m^T+\mathbf{g}_m^T)\big)\mathbf{w}_k \qquad k = p+1,\ldots,2n \tag{3.4}$$

A non-trivial solution is $\mathbf{w}_k = \mathbf{v}_k$ for $k = p+1,\ldots,2n$, so from equations (3.1)

$$\big(\mathbf{b}_1(\lambda_k\mathbf{f}_1^T + \mathbf{g}_1^T) + \ldots + \mathbf{b}_m(\lambda_k\mathbf{f}_m^T + \mathbf{g}_m^T)\big)\mathbf{v}_k = 0 \qquad k = p+1,\ldots,2n \tag{3.5}$$

Otherwise, considering the first p equations that correspond to the p poles to change, equation (3.3) can be written as

$$\mathbf{w}_k = (\mu_k^2\mathbf{M}+\mu_k\mathbf{C}+\mathbf{K})^{-1}\big(\mathbf{b}_1(\mu_k\mathbf{f}_1^T+\mathbf{g}_1^T)+\ldots+\mathbf{b}_m(\mu_k\mathbf{f}_m^T+\mathbf{g}_m^T)\big)\mathbf{w}_k \qquad k = 1,\ldots,p \tag{3.6}$$

The receptance matrix is defined as the inverse of the dynamic stiffness, so

$$\mathbf{H}(s) = (s^2\mathbf{M} + s\mathbf{C} + \mathbf{K})^{-1} \tag{3.7}$$

where s is a general eigenvalue. Therefore

$$\mathbf{w}_k = \mathbf{H}(\mu_k)\big(\mathbf{b}_1(\mu_k\mathbf{f}_1^T + \mathbf{g}_1^T) + \ldots + \mathbf{b}_m(\mu_k\mathbf{f}_m^T + \mathbf{g}_m^T)\big)\mathbf{w}_k \qquad k = 1,\ldots,p \tag{3.8}$$

Denote

$$\mathbf{r}_{\mu_k,j} = \mathbf{H}(\mu_k)\mathbf{b}_j \qquad k = 1,\ldots,p \qquad j = 1,\ldots,m \tag{3.9}$$

and

$$\alpha_{\mu_k,j} = (\mu_k\mathbf{f}_j^T + \mathbf{g}_j^T)\mathbf{w}_k \qquad k = 1,\ldots,p \qquad j = 1,\ldots,m \tag{3.10}$$

so equations (3.8) are composed as a linear combination of $\mathbf{r}_{\mu_k,j}$, and they are

$$\mathbf{w}_k = \alpha_{\mu_k,1}\mathbf{r}_{\mu_k,1} + \ldots + \alpha_{\mu_k,m}\mathbf{r}_{\mu_k,m}, \qquad k = 1,\ldots,p \tag{3.11}$$

In matrix form, equations (3.10) are written as

$$\begin{bmatrix} \mu_k\mathbf{w}_k^T & 0 & \cdots & 0 & \mathbf{w}_k^T & 0 & \cdots & 0 \\ 0 & \mu_k\mathbf{w}_k^T & \cdots & 0 & 0 & \mathbf{w}_k^T & \cdots & 0 \\ \vdots & \vdots & \ddots & \vdots & \vdots & \vdots & \ddots & \vdots \\ 0 & 0 & \cdots & \mu_k\mathbf{w}_k^T & 0 & 0 & \cdots & \mathbf{w}_k^T \end{bmatrix} \begin{pmatrix} \mathbf{f}_1 \\ \vdots \\ \mathbf{f}_m \\ \mathbf{g}_1 \\ \vdots \\ \mathbf{g}_m \end{pmatrix} = \begin{pmatrix} \alpha_{\mu_k,1} \\ \alpha_{\mu_k,2} \\ \vdots \\ \alpha_{\mu_k,m} \end{pmatrix} \tag{3.12}$$

or, in a simple notation

$$\mathbf{P}_k \mathbf{y} = \boldsymbol{\alpha}_k \qquad k = 1, \ldots, p \tag{3.13}$$

For the other $2n - p$ equations, since $b \neq 0$, equations (3.5) become, in matrix form

$$\begin{bmatrix} \lambda_k \mathbf{v}_k^T & 0 & \cdots & 0 & \mathbf{v}_k^T & 0 & \cdots & 0 \\ 0 & \lambda_k \mathbf{v}_k^T & \cdots & 0 & 0 & \mathbf{v}_k^T & \cdots & 0 \\ \vdots & \vdots & \ddots & \vdots & \vdots & \vdots & \ddots & \vdots \\ 0 & 0 & \cdots & \lambda_k \mathbf{v}_k^T & 0 & 0 & \cdots & \mathbf{v}_k^T \end{bmatrix} \begin{pmatrix} \mathbf{f}_1 \\ \vdots \\ \mathbf{f}_m \\ \mathbf{g}_1 \\ \vdots \\ \mathbf{g}_m \end{pmatrix} = \begin{pmatrix} 0 \\ 0 \\ \vdots \\ 0 \end{pmatrix} \tag{3.14}$$

or, in a simple notation

$$\mathbf{Q}_k \mathbf{y} = \mathbf{0} \qquad k = p + 1, \ldots, 2n \tag{3.15}$$

Combining matrices (3.13) with (3.15), the system of linear equations to be solved is

$$\begin{bmatrix} \mathbf{P}_1 \\ \vdots \\ \mathbf{P}_p \\ \mathbf{Q}_{p+1} \\ \vdots \\ \mathbf{Q}_{2n} \end{bmatrix} \begin{pmatrix} \mathbf{f}_1 \\ \vdots \\ \mathbf{f}_m \\ \mathbf{g}_1 \\ \vdots \\ \mathbf{g}_m \end{pmatrix} = \begin{pmatrix} \boldsymbol{\alpha}_1 \\ \vdots \\ \boldsymbol{\alpha}_p \\ \mathbf{0} \\ \vdots \\ \mathbf{0} \end{pmatrix} \tag{3.16}$$

Thus, the gains f_j and g_j are determined by choosing $\alpha_{\mu_k,j}$, obtaining $\mathbf{w}_k$ from the control vectors b_j and the measured receptance $\mathbf{H}(\mu_k)$ at the desired poles μ_k (for $k = 1, \ldots, p$ and $j = 1, \ldots, m$) and calculating the eigenpairs of the system λ_k and $\mathbf{v}_k$ (for $k = p+1, \ldots, 2n$).

With this method, there is no need to evaluate the properties of the system such as $\mathbf{M}$, $\mathbf{C}$ and $\mathbf{K}$ matrices, because the receptance matrix can be computed from the system's response. Note also that, if $\mathbf{F}$ and $\mathbf{G}$ are real and $\mathbf{w}$ and μ are an eigenpair, also the complex conjugation $\overline{\mathbf{w}}$ and $\overline{\mu}$ are an eigenpair, so from equations (3.10) the choice of $\alpha_{\mu_k,j} = \overline{\alpha}_{\overline{\mu}_k,j}$ gives real values of $\mathbf{F}$ and $\mathbf{G}$.

In section 4 of [22] is also expressed a way to choose the arbitrary parameters $\boldsymbol{\alpha}_k$ by imposing modal constraints. From (3.10), the imposition

$$(\mu_k \mathbf{f}_m^T + \mathbf{g}_m^T)\mathbf{w}_k = 1 \qquad k = 1, \ldots, p \tag{3.17}$$

gives

$$\alpha_{\mu_k,m} = 1 \qquad k = 1, \ldots, p \tag{3.18}$$

for each assigned pole μ_k. With the nodal constraint $w_{k,j} = 0$, the other arbitrary parameters are determined by

$$\mathbf{e}_j^T \mathbf{R}_k \boldsymbol{\alpha}_k = \mathbf{0} \qquad k = 1, \ldots, p \qquad j = 1, \ldots, m-1 \tag{3.19}$$

where $\mathbf{e}_j$ is the j-th unit vector, $\mathbf{R}_k$ is the matrix composed by $\mathbf{r}_{\mu_k}$ vectors, so

$$\mathbf{R}_k = [\mathbf{r}_{\mu_k,1} \quad \cdots \quad \mathbf{r}_{\mu_k,m}] \qquad k = 1, \ldots, p \tag{3.20}$$

and $\boldsymbol{\alpha}_k$ is

$$\boldsymbol{\alpha}_k^T = (\alpha_{\mu_k,1} \quad \cdots \quad \alpha_{\mu_k,m-1} \quad 1) \qquad k = 1, \ldots, p \tag{3.21}$$

In this way, by the $m-1$ equations (3.19) it is possible to determine all the $m-1$ parameters for each pole μ_k.

It is also possible to impose a modal ratio constraint ρ corresponding to

$$\rho = \frac{w_{k,i}}{w_{k,j}} \qquad k = 1, \ldots, p \qquad i = 1, \ldots, m-1 \qquad j = 1, \ldots, m-1 \tag{3.22}$$

and the system of equations to solve is

$$(\mathbf{e}_i^T - \rho \mathbf{e}_j^T)\mathbf{R}_k \boldsymbol{\alpha}_k = \mathbf{0} \qquad k = 1, \ldots, p \quad i = 1, \ldots, m-1 \quad i \neq j = 1, \ldots, m \tag{3.23}$$

3.1.2 Example of receptance method application

An example easily explains what happens to a system when the receptance method is applied. So, let consider a system with 2 DoFs, composed by 2 masses m_i for $i = 1, 2$, dampers c_j and springs k_j for $j = 1, 2, 3$, as shown in Figure 3.1. The open loop system of equations is the follow

$$\begin{cases} m_1\ddot{x}_1 + c_1\dot{x}_1 + c_2(\dot{x}_1 - \dot{x}_2) + k_1x_1 + k_2(x_1 - x_2) = 0 \\ m_2\ddot{x}_2 + c_3\dot{x}_2 + c_2(\dot{x}_2 - \dot{x}_1) + k_3x_2 + k_2(x_2 - x_1) = 0 \end{cases} \tag{3.24}$$

where x_i for $i = 1, 2$ are the displacements of the two Degrees of Freedom, $\dot{x}_i$ is the first time derivative, so the velocity and $\ddot{x}_i$ is the acceleration of the DoFs. Equations (3.24) can be grouped by $x_i, \dot{x}_i, \ddot{x}_i$, so

$$\begin{cases} m_1\ddot{x}_1 + (c_1 + c_2)\dot{x}_1 - c_2\dot{x}_2 + (k_1 + k_2)x_1 - k_2x_2 = 0 \\ m_2\ddot{x}_2 - c_2\dot{x}_1 + (c_2 + c_3)\dot{x}_2 - k_2x_1 + (k_2 + k_3)x_2 = 0 \end{cases} \tag{3.25}$$

and in matrix form

$$\begin{bmatrix} m_1 & 0 \\ 0 & m_2 \end{bmatrix} \begin{pmatrix} \ddot{x}_1 \\ \ddot{x}_2 \end{pmatrix} + \begin{bmatrix} c_1 + c_2 & -c_2 \\ -c_2 & c_2 + c_3 \end{bmatrix} \begin{pmatrix} \dot{x}_1 \\ \dot{x}_2 \end{pmatrix} + \begin{bmatrix} k_1 + k_2 & -k_2 \\ -k_2 & k_2 + k_3 \end{bmatrix} \begin{pmatrix} x_1 \\ x_2 \end{pmatrix} = \begin{pmatrix} 0 \\ 0 \end{pmatrix} \tag{3.26}$$

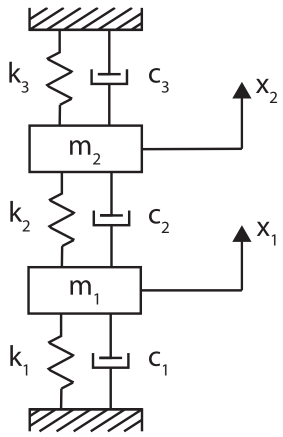

Figure 3.1: Mass-spring-damper system with 2 DoFs

so

$$\mathbf{M}\ddot{\mathbf{q}} + \mathbf{C}\dot{\mathbf{q}} + \mathbf{K}\mathbf{q} = \mathbf{0} \tag{3.27}$$

where $\mathbf{q}$ is the DoFs vector. Applying the receptance method, the closed loop system is

$$\mathbf{M}\ddot{\mathbf{q}} + \mathbf{C}\dot{\mathbf{q}} + \mathbf{K}\mathbf{q} = \mathbf{B}(\mathbf{F}^T\dot{\mathbf{q}} + \mathbf{G}^T\mathbf{q}) \tag{3.28}$$

where $\mathbf{B}$, $\mathbf{F}$ and $\mathbf{G}$, for 2 inputs, are

$$\mathbf{B} = \begin{bmatrix} b_{11} & b_{12} \\ b_{21} & b_{22} \end{bmatrix} \qquad \mathbf{F} = \begin{bmatrix} f_{11} & f_{12} \\ f_{21} & f_{22} \end{bmatrix} \qquad \mathbf{G} = \begin{bmatrix} g_{11} & g_{12} \\ g_{21} & g_{22} \end{bmatrix} \tag{3.29}$$

This means that the gains modify the damping and stiffness of the system, leading to a movement of its poles in the required position. Moving terms of (3.28), the new system becomes

$$\mathbf{M}\ddot{\mathbf{q}} + (\mathbf{C} - \mathbf{B}\mathbf{F}^T)\dot{\mathbf{q}} + (\mathbf{K} - \mathbf{B}\mathbf{G}^T)\mathbf{q} = \mathbf{0} \tag{3.30}$$

The same example as presented in [22] is now repeated, giving values to the system's elements: $m_1 = 1\,\mathrm{kg}$ and $m_2 = 2\,\mathrm{kg}$ for the masses, $c_1 = 0\,\mathrm{N\,s\,m^{-1}}$, $c_2 = 5\,\mathrm{N\,s\,m^{-1}}$ and $c_3 = 0\,\mathrm{N\,s\,m^{-1}}$ for the dampers, $k_1 = 5\,\mathrm{N\,m^{-1}}$, $k_2 = 5\,\mathrm{N\,m^{-1}}$ and $k_3 = 10\,\mathrm{N\,m^{-1}}$ for the springs. Therefore, by (3.26)

$$\mathbf{M} = \begin{bmatrix} 1 & 0 \\ 0 & 2 \end{bmatrix} \qquad \mathbf{C} = \begin{bmatrix} 5 & -5 \\ -5 & 5 \end{bmatrix} \qquad \mathbf{K} = \begin{bmatrix} 10 & -5 \\ -5 & 15 \end{bmatrix}$$

The eigenpairs of the system are the follows

$$\left\{ \lambda_{1,2} = \pm\sqrt{5}i \quad \mathbf{v}_{1,2} = \begin{pmatrix} 1 \\ 1 \end{pmatrix} \right\} \qquad \left\{ \lambda_3 = -2.5 \quad \mathbf{v}_3 = \begin{pmatrix} 2 \\ -1 \end{pmatrix} \right\} \qquad \left\{ \lambda_4 = -5 \quad \mathbf{v}_4 = \begin{pmatrix} 2 \\ -1 \end{pmatrix} \right\}$$

While $\lambda_{1,2}$ will be changed with the new poles $\mu_{1,2} = -1 \pm i$, λ_3 and λ_4 will be kept unchanged. The input matrix is chosen to be

$$\mathbf{B} = \begin{bmatrix} 1 & 1 \\ 0 & -2 \end{bmatrix}$$

Moreover, the arbitrary parameters are

$$\alpha_{\mu_k,1} = 1 \qquad \alpha_{\mu_k,2} = 0.5 \qquad k = 1,2$$

knowing that the choice of $\alpha_{\mu_k,j}$ determines the eigenvectors of assigned modes by (3.11). Now it is possible to compute the receptance matrix as in (3.7) and then **r** and **w** respectively from (3.9) and (3.11). Applying (3.16), the gain matrices needed to perform the closed loop are

$$\mathbf{F} = \begin{bmatrix} -4 & -2 \\ -8 & -4 \end{bmatrix} \qquad \mathbf{G} = \begin{bmatrix} 6 & 3 \\ 12 & 6 \end{bmatrix}$$

and the closed loop becomes

$$\begin{bmatrix} 1 & 0 \\ 0 & 2 \end{bmatrix} \begin{pmatrix} \ddot{x}_1 \\ \ddot{x}_2 \end{pmatrix} + \begin{bmatrix} 11 & 7 \\ -9 & -3 \end{bmatrix} \begin{pmatrix} \dot{x}_1 \\ \dot{x}_2 \end{pmatrix} + \begin{bmatrix} 1 & -23 \\ 1 & 27 \end{bmatrix} \begin{pmatrix} x_1 \\ x_2 \end{pmatrix} = \begin{pmatrix} 0 \\ 0 \end{pmatrix}$$

Note how the symmetry of **C** and **K** is lost.

3.2 MATLAB algorithm of the receptance method

The receptance method was implemented in MATLAB. The algorithm developed can determine the feedback gains for systems with any number of DoFs and inputs. Moreover, by making use of *state-space* model, the receptance matrix computation does not need structural matrices of the system, but only its transfer functions.

3.2.1 State-space model

Working in the state-space form, differential equations of a dynamic system are rewritten as a set of first-order differential equations. The system variables become state-variables, which represent the so-called system *states*. The states could be defined in different way, but they have to be sufficient to represent the dynamic behaviour of the system.

Consider a dynamic system described as

$$\mathbf{M\ddot{q}} + \mathbf{C\dot{q}} + \mathbf{Kq} = \mathbf{Bu} \tag{3.31}$$

where **u** is the input vector, with m rows. The isolation of $\ddot{\mathbf{q}}$ gives

$$\ddot{\mathbf{q}} = -\mathbf{M}^{-1}(\mathbf{C\dot{q}} + \mathbf{Kq}) + \mathbf{M}^{-1}\mathbf{Bu} \tag{3.32}$$

which may be written in matrix form as

$$\begin{pmatrix} \dot{\mathbf{q}} \\ \ddot{\mathbf{q}} \end{pmatrix} = \begin{bmatrix} \mathbf{0} & \mathbf{I} \\ -\mathbf{M}^{-1}\mathbf{K} & -\mathbf{M}^{-1}\mathbf{C} \end{bmatrix} \begin{pmatrix} \mathbf{q} \\ \dot{\mathbf{q}} \end{pmatrix} + \begin{bmatrix} \mathbf{0} \\ \mathbf{M}^{-1}\mathbf{B} \end{bmatrix} \mathbf{u} \tag{3.33}$$

where $\mathbf{I}$ is the identity matrix. In a compressed form, the previous equation is expressed as

$$\dot{\mathbf{x}} = \mathbf{A_{ss}}\mathbf{x} + \mathbf{B_{ss}}\mathbf{u} \tag{3.34}$$

The vector $\mathbf{x} = (\mathbf{q} \quad \dot{\mathbf{q}})^T$ is called *state of the system* because it contains the system states. In this case, it contains $2n$ elements because it consists of displacements and velocities of the n DoFs. $\mathbf{A_{ss}} \in \mathbb{R}^{2n\times 2n}$ is the *system matrix* while $\mathbf{B_{ss}} \in \mathbb{R}^{2n\times m}$ is the *input matrix*.

On the other hand, the DoFs displacements are chosen as outputs, so $\mathbf{y} = \mathbf{q}$. In matrix form it is

$$\mathbf{y} = \begin{bmatrix} \mathbf{I} & \mathbf{0} \end{bmatrix} \begin{pmatrix} \mathbf{q} \\ \dot{\mathbf{q}} \end{pmatrix} + \mathbf{0} \cdot \mathbf{u} \tag{3.35}$$

or

$$\mathbf{y} = \mathbf{C_{ss}}\mathbf{x} + \mathbf{D_{ss}}\mathbf{u} \tag{3.36}$$

where $\mathbf{C_{ss}} \in \mathbb{R}^{l\times 2n}$ is the *output matrix* and $\mathbf{D_{ss}} \in \mathbb{R}^{l\times m}$ is the *direct transmission matrix.*[1]. In this case $\mathbf{y} = \mathbf{q}$, so $l = n$. Equations (3.34) and (3.36) are known as *state-space equations*. This method is used for feedback control systems design and it makes easier to extend the system to more inputs or outputs.

In state-space form, eigenvalues of the system can be found from $\mathbf{A_{ss}}$ matrix. In fact, by considering the system without input terms

$$\dot{\mathbf{x}} = \mathbf{A_{ss}}\mathbf{x} \quad \rightarrow \quad \dot{\mathbf{x}} - \mathbf{A_{ss}}\mathbf{x} = \mathbf{0} \tag{3.37}$$

With a solution for the state vector like

$$\mathbf{x} = \mathbf{x_0} e^{\lambda t} \tag{3.38}$$

equation (3.37) becomes

$$\lambda\mathbf{x_0} - \mathbf{A_{ss}}\mathbf{x_0} = \mathbf{0} \quad \rightarrow \quad (\lambda\mathbf{I} - \mathbf{A_{ss}})\mathbf{x_0} = \mathbf{0} \quad \rightarrow \quad (\mathbf{A_{ss}} - \lambda\mathbf{I})\mathbf{x_0} = \mathbf{0} \tag{3.39}$$

which is in the classical eigensolution form.

[1]Usually the notation is $\mathbf{A}$, $\mathbf{B}$, $\mathbf{C}$ and $\mathbf{D}$ instead of $\mathbf{A_{ss}}$, $\mathbf{B_{ss}}$, $\mathbf{C_{ss}}$ and $\mathbf{D_{ss}}$, but the second one is here used to differentiate them from the control force distribution and the damping matrices.

About the transfer function, the Laplace transform of (3.34) is

$$s\mathbf{x}(s) = \mathbf{A_{ss}}\mathbf{x}(s) + \mathbf{B_{ss}}\mathbf{u}(s) \quad \rightarrow \quad \mathbf{x}(s) = [s\mathbf{I} - \mathbf{A_{ss}}]^{-1}\mathbf{B_{ss}}\mathbf{u}(s) \tag{3.40}$$

Substitution of it inside the Laplace transform of (3.36), gives

$$\mathbf{y}(s) = (\mathbf{C_{ss}}[s\mathbf{I} - \mathbf{A_{ss}}]^{-1}\mathbf{B_{ss}} + \mathbf{D_{ss}})\mathbf{u}(s) = \mathbf{T}(s)\mathbf{u}(s) \tag{3.41}$$

where $\mathbf{T}(s)$ is a matrix of transfer functions, which contains the ratios from each output to each input.

3.2.2 MATLAB algorithm

The state-space model is implemented in MATLAB by creating the $\mathbf{A_{ss}}$, $\mathbf{B_{ss}}$, $\mathbf{C_{ss}}$ and $\mathbf{D_{ss}}$ matrices from the structural matrices, as in equations (3.33) and (3.35). However, these 4 matrices can be also computed from a numerical model, as done from the MODFLEX wing numerical model in chapter 4, so, in reality, there is no need to know the $\mathbf{M}$, $\mathbf{C}$ and $\mathbf{K}$ structural matrices. Furthermore, it is possible to determine a state-space formulation also from experimental FRFs, as described in chapter 5.

The matrix of transfer functions $\mathbf{T}(s)$, obtained from the equations in state-space form, is the product of the receptance matrix and the control force distribution matrix. Indeed, by considering an open loop eigenvalue problem of a mass-spring-damper system

$$(s^2\mathbf{M} + s\mathbf{C} + \mathbf{K})\mathbf{q}(s) = \mathbf{B}\mathbf{u}(s) \tag{3.42}$$

the transfer function is the ratio between the outputs and the inputs, which here are respectively $\mathbf{q}(s)$ and $\mathbf{u}(s)$. Therefore, also by the receptance matrix in equation (3.7), the transfer function matrix is

$$\mathbf{T}(s) = \frac{\mathbf{q}(s)}{\mathbf{u}(s)} = (s^2\mathbf{M} + s\mathbf{C} + \mathbf{K})^{-1}\mathbf{B} = \mathbf{H}(s)\mathbf{B} = \mathbf{r}_s \tag{3.43}$$

The transfer function is then used for the computation of the eigenvectors $\mathbf{w}_k$ of each desired pole μ_k, as equation (3.11). If the system is complicated and it is not possible to know its natural eigenvectors $\mathbf{v}_k$, the transfer function can be also used for the evaluation of them. Indeed, from the example in section 3.1.2, the eigenvectors of the system are

$$\mathbf{v}_{1,2} = \begin{pmatrix} 1 \\ 1 \end{pmatrix} \qquad \mathbf{v}_3 = \begin{pmatrix} 2 \\ -1 \end{pmatrix} \qquad \mathbf{v}_4 = \begin{pmatrix} 2 \\ -1 \end{pmatrix}$$

while, by calculating the transfer function at the natural eigenvalues, so for $s = \lambda_k$, the matrices obtained are proportional to

$$\mathbf{r}_{1,2} = \begin{bmatrix} (-8.3772 \mp 0.7493i) & (8.3772 \pm 0.7493i) \\ (-8.3772 \mp 0.7493i) & (8.3772 \pm 0.7493i) \end{bmatrix}$$

$$\mathbf{r}_3 = \begin{bmatrix} -0.5278 & -1.0555 \\ 0.2639 & 0.5278 \end{bmatrix} \qquad \mathbf{r}_4 = \begin{bmatrix} -0.5629 & -1.1259 \\ 0.2815 & 0.5629 \end{bmatrix}$$

They have 2 columns because of the 2 inputs and 2 rows because of the 2 outputs, but the ratio between the first and the second row is the same for each column, and it is equal to $\mathbf{v}_k$. Thus, it results

$$\mathbf{r}_{\lambda_k,i} = CONST \cdot \mathbf{r}_{\lambda_k,j} \qquad i = 1,\ldots,m \quad j = 1,\ldots,m \tag{3.44}$$

So, just one column of the transfer function can be used as eigenvector of the system, because it is proportional to $\mathbf{v}_k$.

In conclusion, **F** and **G** feedback gain matrices can be obtained by the computation of the state-space matrices, the selection of the retained and substituted poles and the choice of $\boldsymbol{\alpha}_k$.

3.2.3 Example with the state-space model

The example in section 3.1.2 can be rewritten with the state-space model by using equations (3.33) and (3.35), so obtaining

$$\mathbf{A_{ss}} = \begin{bmatrix} 0 & 0 & 1 & 0 \\ 0 & 0 & 0 & 1 \\ -10 & 5 & -5 & 5 \\ 2.5 & -7.5 & 2.5 & -2.5 \end{bmatrix} \qquad \mathbf{B_{ss}} = \begin{bmatrix} 0 & 0 \\ 0 & 0 \\ 1 & 1 \\ 0 & -1 \end{bmatrix}$$

$$\mathbf{C_{ss}} = \begin{bmatrix} 1 & 0 & 0 & 0 \\ 0 & 1 & 0 & 0 \end{bmatrix} \qquad \mathbf{D_{ss}} = \begin{bmatrix} 0 & 0 \\ 0 & 0 \end{bmatrix}$$

From the state-space system, 4 Bode diagrams can be drawn, which represent the FRFs of each output forced by each input. All of them are shown in Figure 3.2, in dotted line. Each top diagram represents the magnitude of the response calculated in decibel (dB), while each bottom diagram is the phase in degrees (deg). They come from the transfer function calculated for $s = \omega i$, where ω is the excitation frequency. For each considered frequency, the transfer function between 1 input and 1 output returns a complex value composed by a real and an imaginary part, so

$$\mathbf{r}_{\omega i} = Re(\omega) \pm Im(\omega)i \tag{3.45}$$

From these, magnitude and phase of the response can be simply obtained by

$$magnitude\,[\text{dB}] = 20\log_{10}(\sqrt{Re^2 + Im^2}) \tag{3.46}$$

$$phase\,[\text{rad}] = \arctan\left(\frac{Im}{Re}\right) \quad \rightarrow \quad phase\,[\text{deg}] = phase\,[\text{rad}] \cdot \frac{180}{\pi} \tag{3.47}$$

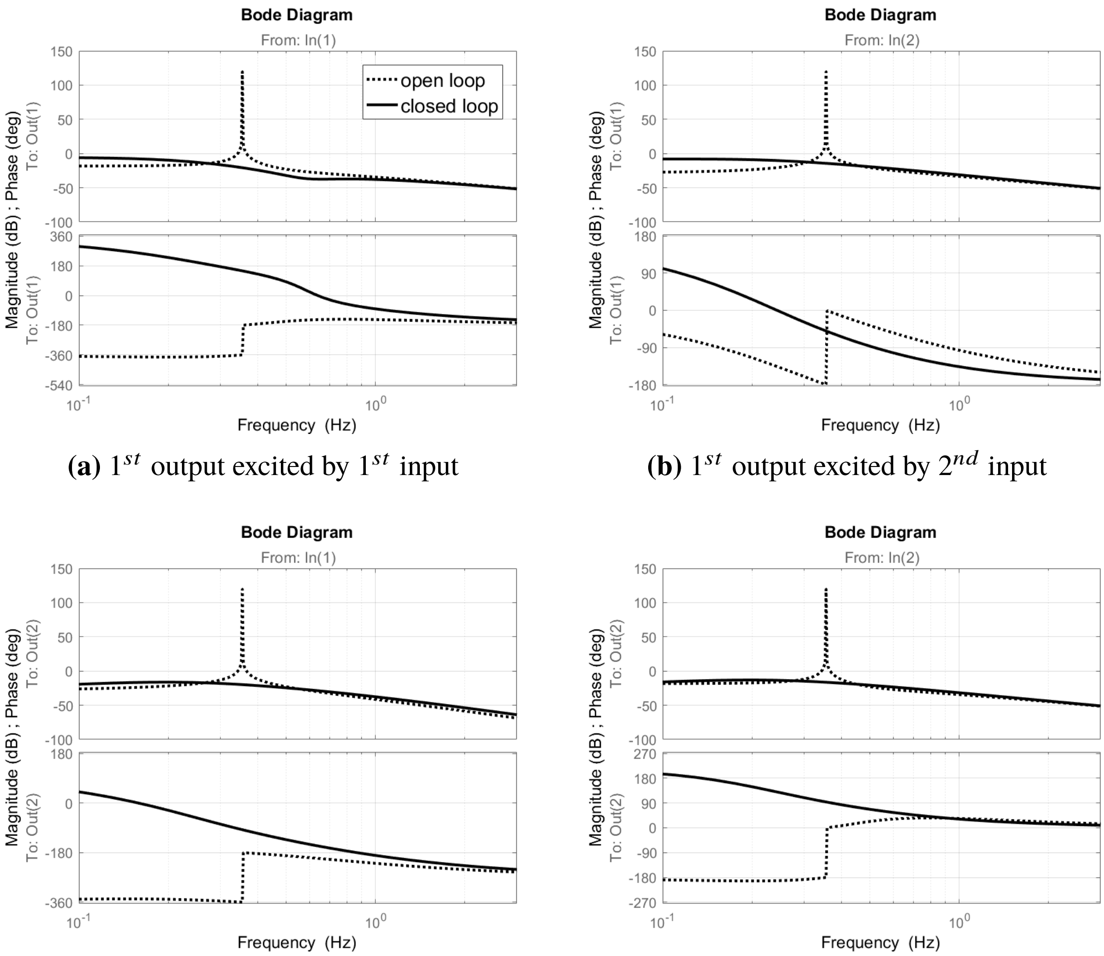

(a) 1^{st} output excited by 1^{st} input

(b) 1^{st} output excited by 2^{nd} input

(c) 2^{nd} output excited by 1^{st} input

(d) 2^{nd} output excited by 2^{nd} input

Figure 3.2: Bode diagrams of a mass-spring-damper system. Dotted line represents the open loop, solid line is the closed loop

About the x-axis, the frequency can be expressed in rad/s or in Hz, and the relation between them is

$$\textit{frequency}\,[\text{rad/s}] = \textit{frequency}\,[\text{Hz}] \cdot 2\pi \tag{3.48}$$

For this case the frequencies are in Hz in a range from 0.1 to 3 Hz. The MATLAB function of the receptance method gives the same **F** and **G** matrices of the previous described example. The inputs for the closed loop system are

$$\mathbf{u} = (\mathbf{F}^T\dot{\mathbf{q}} + \mathbf{G}^T\mathbf{q}) \tag{3.49}$$

and thus the terms of the $\mathbf{B_{ss}}$ matrix can be added to $\mathbf{A_{ss}}$. From equation (3.33), the system matrix becomes

$$\mathbf{A_{ss}}_{CL} = \begin{bmatrix} \mathbf{0} & \mathbf{I} \\ -\mathbf{M^{-1}K} + \mathbf{M^{-1}BG}^T & -\mathbf{M^{-1}C} + \mathbf{M^{-1}BF}^T \end{bmatrix} \tag{3.50}$$

or with numbers, for this example

$$\mathbf{A_{ss}}_{CL} = \begin{bmatrix} 0 & 0 & 1 & 0 \\ 0 & 0 & 0 & 1 \\ -1 & 23 & -11 & -7 \\ -0.5 & -13.5 & 4.5 & 1.5 \end{bmatrix}$$

Bode diagrams of the system controlled in closed loop are shown in Figure 3.2, in solid line. The open loop poles $\lambda_{1,2} = \pm\sqrt{5}i$ are without damping, resulting in a peak in the module response, since the desired poles $\mu_{1,2} = -1 \pm i$ have high damping, no clear peaks are visible for the closed loop.

Chapter 4

Control analysis of the wing numerical model

The numerical model of the MODFLEX wing was used to get its state-space formulation, which represents the response of the wing inside an airstream with a velocity of 10 m/s. The purpose was to use it in MATLAB and to find **F** and **G** gains, by applying the receptance method.

4.1 Control design

The state-space formulation of the wing has 2 inputs (2 control surfaces) and 4 outputs (2 laser sensors and 2 encoders of the brushless motors). This system results unstable because the leading edge control surface of the numerical model has no stiffness, so every angle different from zero degrees leads to an aerodynamic force not balanced, resulting in an increase of rotation because of the upfront wind. This instability is removed with a Linear Time-Invariant (LTI) Simulink block applied to the leading edge input on the Simulink wing model, with a feedback from the leading edge encoder. It was setted with the MATLAB `sisotool` Toolbox. The LTI block is so a transfer function with 2 zeros and 2 poles, corresponding to

$$LTI(s) = g\frac{(s+p_1)(s+p_2)}{(s+z_1)(s+z_2)} = 19.455\frac{(s+148.7)(s+13.01)}{s(s+14540)}$$

where p_i, z_i and g are the poles, zeros and gain of the transfer function. In Figure 4.1 there is the Simulink control model with the LTI block on an inner loop.

Both the encoders are used to set PID controllers as done for the experimental model. The Simulink model which shows this loop is presented in Figure 4.2, in which the "StableSystem" block includes the inner loop of Figure 4.1. PID controllers are used to have faster and more accurate response of control surfaces' motors after an input command. They were manually tuned by observing both the responses in time and in

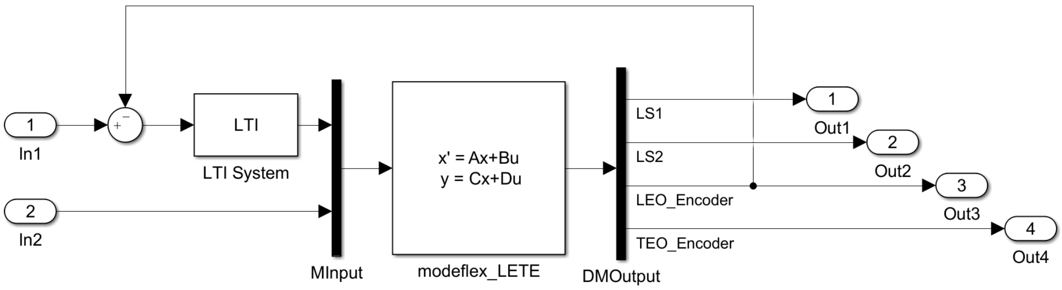

Figure 4.1: Inner loop of the Simulink wing model

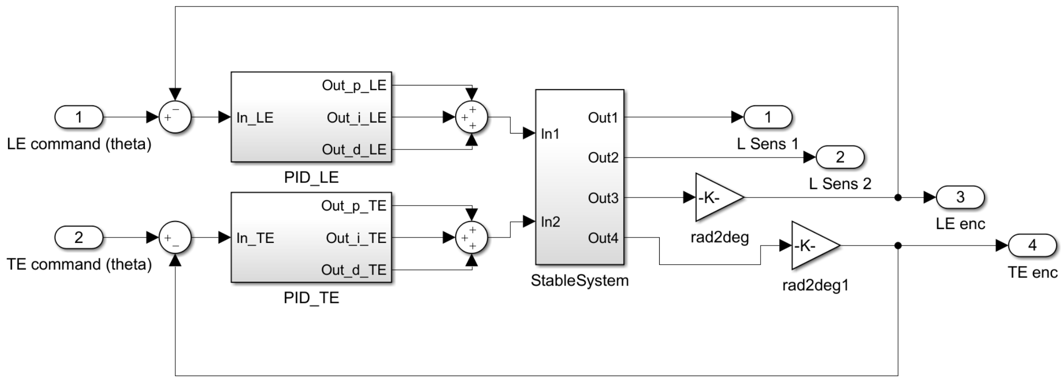

Figure 4.2: Outer loop of the Simulink wing model

frequency domain. Thus, the selected gain values for the controller connected to the leading edge input are

$$K_P = 0.2 \qquad K_I = 3 \qquad K_D = 0.001$$

while, for the controller connected to the trailing edge input they are

$$K_P = 0.01 \qquad K_I = 0.1 \qquad K_D = 0.0001$$

Bode diagrams of the encoder readings from their input (LE encoder reading from LE command and TE encoder reading from TE command) are presented in Figure 4.3a and in Figure 4.3b respectively, with and without the PID controllers. Frequency range is from 1 to 10^5 Hz. The PID controllers remove the peaks visible at high frequency. Responses of the motors in time domain registered by the encoders are in Figures 4.4, with and without the PID controllers. They show the reaction after a step command of 1 degree. The controller removes the vibration of the motors after a command, but increased a little the time delay.

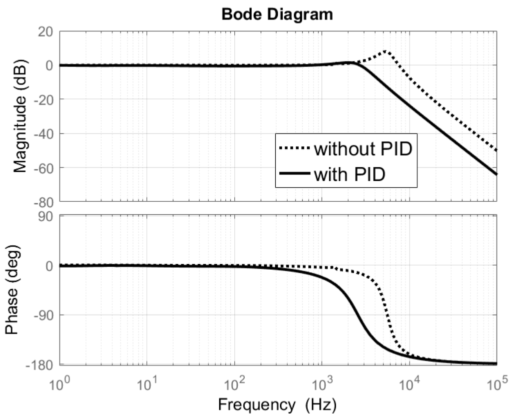

(a) LE command to LE encoder

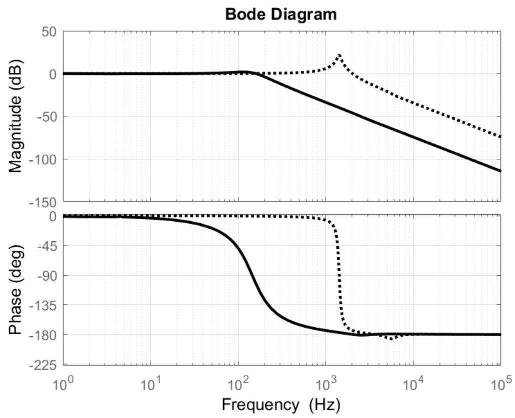

(b) TE command to TE encoder

Figure 4.3: Bode diagrams of the encoder readings for the wing numerical model. Dotted lines represent the response without the PID controller, solid lines with it

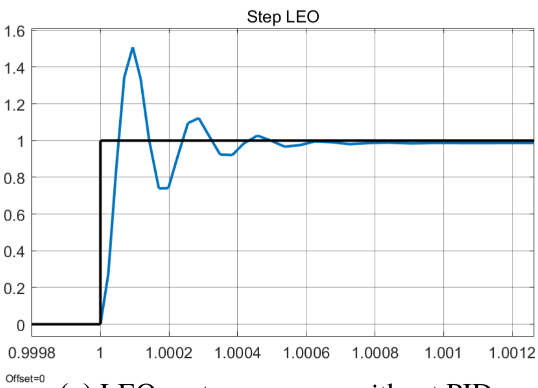

(a) LEO motor response without PID

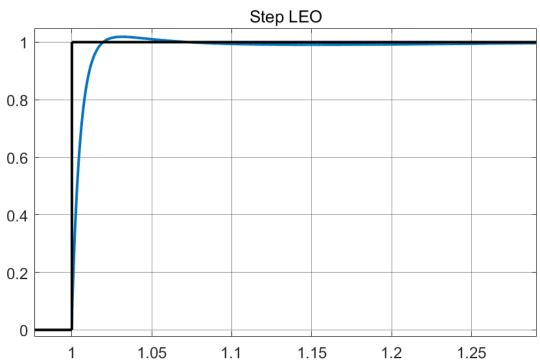

(b) LEO motor response with PID

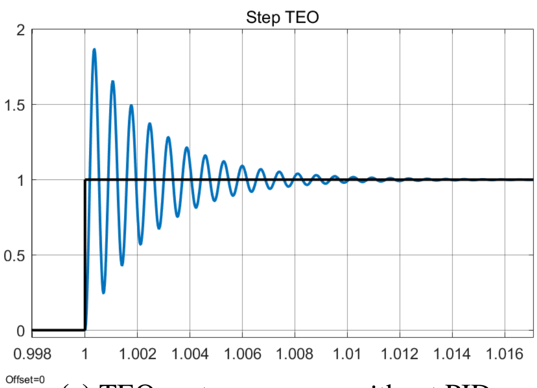

(c) TEO motor response without PID

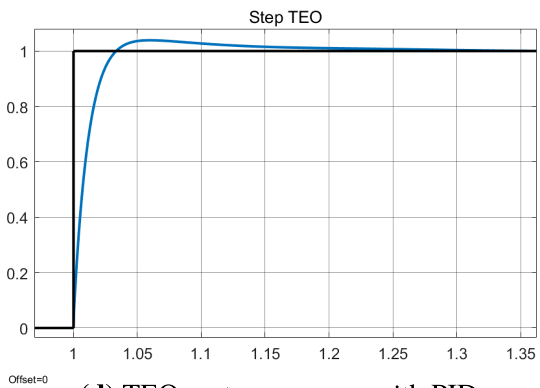

(d) TEO motor response with PID

Figure 4.4: LEO and TEO motor response in time domain after a step command for the wing numerical model. Black line is the command, blue line is the response

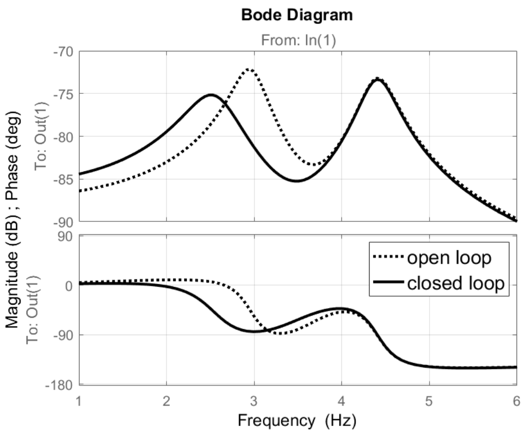

(a) 1^{st} output excited by 1^{st} input

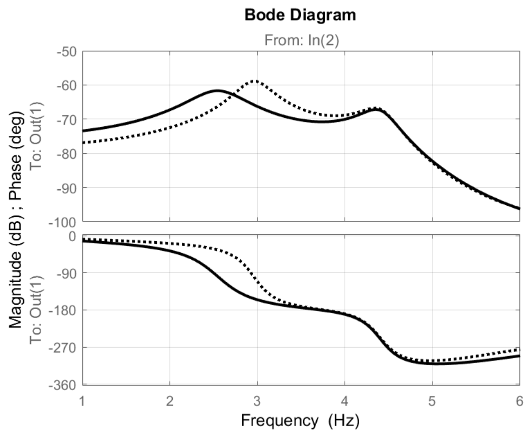

(b) 1^{st} output excited by 2^{nd} input

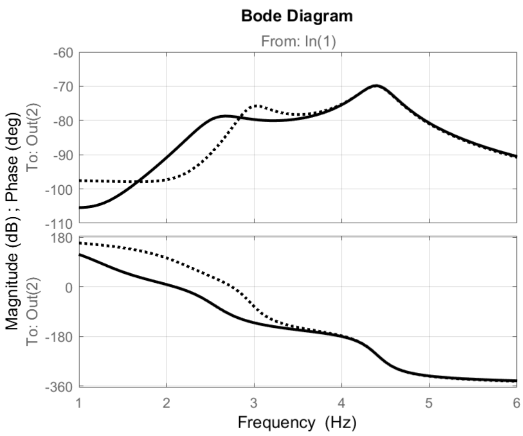

(c) 2^{nd} output excited by 1^{st} input

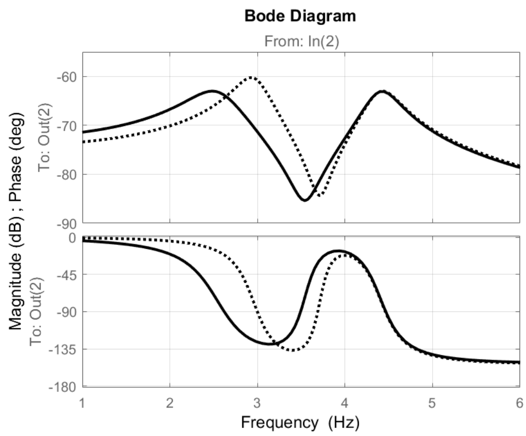

(d) 2^{nd} output excited by 2^{nd} input

Figure 4.5: Bode diagrams of the wing numerical model. Dotted line represents the open loop, solid line is the closed loop

4.2 Example of one system pole placement

The open loop system response, registered by its outputs when excited by each input is shown in Figure 4.5, in dotted line, by using Bode diagrams. Frequency range is between 1 and 6 Hz. 1^{st} and 2^{nd} inputs are respectively the LE and TE control surfaces commands, while 1^{st} and 2^{nd} outputs are respectively the laser sensor on leading edge and the laser sensor on trailing edge readings.

The system eigenvalues, determined from the $\mathbf{A_{ss}}$ system matrix, are those of the system with also the poles added by the LTI block and by the PID controllers. The system eigenvalues that correspond to the peaks visible in the Bode diagrams are

$$\lambda_{1,2} = -1.25 \pm 18.59i \qquad \lambda_{3,4} = -1.31 \pm 27.67i$$

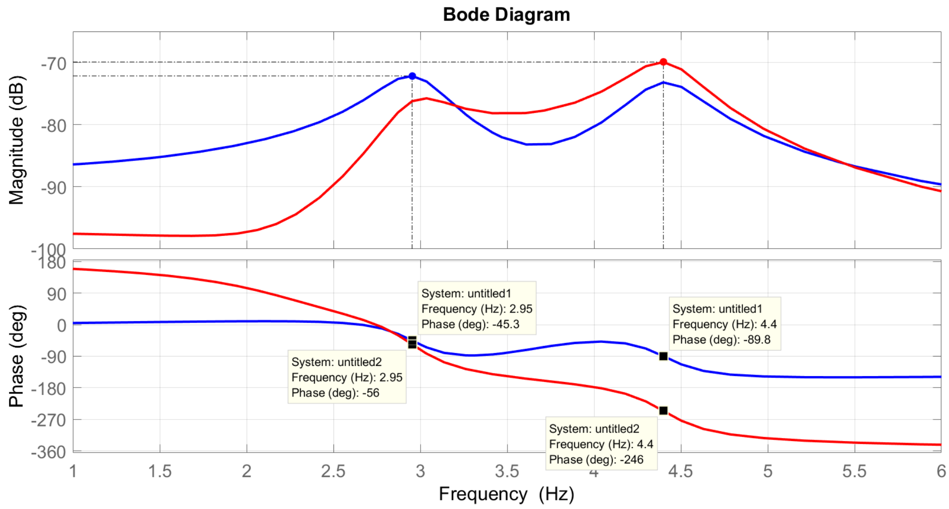

Figure 4.6: Comparison of the 2 outputs of the wing numerical model, excited by the 1^{st} input. Blue line represents the 1^{st} output response, red line is the 2^{nd} output response, both in open loop

They correspond to the first bending and the first torsional modes. Indeed, in Figure 4.6, the 1^{st} output response and the 2^{nd} output response are presented, both commanded by the 1^{st} input. The phases of responses at the first peak are

$$\Phi_{1_1} = -45.3° \qquad \Phi_{1_2} = -56°$$

which means that the two points on the wing where the lasers are positioned are oscillating more or less without phase difference. So this peak shows the resonance corresponding to the first bending mode. At the second peak, the phases are

$$\Phi_{2_1} = -89.8° \qquad \Phi_{2_2} = -246°$$

They have a phase lag close to 180°, so they are in opposition and thus the second peak corresponds to the first torsional mode.

Partial pole placement is done by retaining the complex conjugate couple $\lambda_{3,4}$ and by moving the other couple. It is possible to evaluate the natural eigenvectors from the transfer function of the system $\mathbf{r}_s$ computed at $s = \lambda_i$, with $i = 1, \ldots, 4$. The eigenvectors of the retained poles are then determined in this way, obtaining them proportional to

$$\mathbf{v}_{3,4} = \begin{bmatrix} 0.322 \pm 0.056i \\ -0.502 \mp 0.246i \end{bmatrix}$$

The new poles are placed at

$$\mu_{1,2} = -2 \pm 16i$$

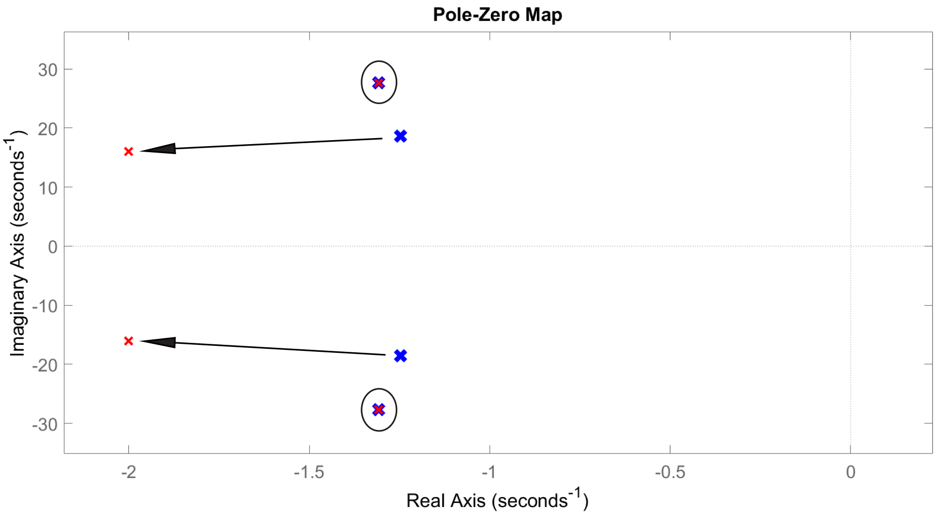

Figure 4.7: Pole-zero map of the wing numerical model. Blue X are the poles in open loop, while red X are the poles in closed loop

in order to increase the damping and to increase the frequency distance to the other couple of poles. About the $\boldsymbol{\alpha}_k$ vector, it may be chosen arbitrarily, so

$$\alpha_{\mu_k,1} = 1 \qquad \alpha_{\mu_k,2} = 0.5 \qquad k = 1,\ldots,2$$

where 1 and 2 subscripts mean the first and the second input.

Applying the receptance method, the control gains obtained are

$$\mathbf{F} = \begin{bmatrix} -33.5 & -16.8 \\ -29.4 & -14.7 \end{bmatrix} \qquad \mathbf{G} = \begin{bmatrix} 1751.7 & 875.9 \\ 819.3 & 409.6 \end{bmatrix}$$

They have values higher than one thousand, which are really high. This is probably because the selected values of $\boldsymbol{\alpha}_k$ move the eigenvectors significantly from the open loop ones, or because a movement in frequency and damping together needs more control authority. However, the closed loop system performed with these gains has new eigenvalues in the desired position. Indeed, Bode plots in Figure 4.5, in solid line, have the first peak at lower frequency and more damped, as desired.

Figure 4.7 shows the pole-zero map, which represents the poles and the zeros of the system in open and closed loop. This figure is intentionally zoomed to show the poles related with the first 2 analysed modes. It displays the shift of the first pole, while the second one remains in the same position. However, all the other system poles have a negative real part, so the system results stable before and after the control strategy.

4.3 Example of only damping increment

4.3.1 Arbitrary choice of α_k

In this case, only the damping of the same couple of eigenvalues is changed, increasing it by 0.15. Hence, the new poles are

$$\mu_{1,2} = -4 \pm 18.28i$$

and $\boldsymbol{\alpha}_k$ is selected arbitrarily again, so

$$\alpha_{\mu_k,1} = 1 \qquad \alpha_{\mu_k,2} = 0.5 \qquad k = 1,\ldots,2$$

The receptance method algorithm gives the following gain matrices

$$\mathbf{F} = \begin{bmatrix} -111.9 & -55.9 \\ -63.7 & -31.9 \end{bmatrix} \qquad \mathbf{G} = \begin{bmatrix} 5.9 & 3.0 \\ -501.1 & -250.6 \end{bmatrix}$$

They are large values as well. Thus, a modal constraint is needed to be sure that the placed eigenvectors are similar to the open loop ones, in order to reduce the gain values.

Bode diagrams of this new closed loop are in Figure 4.8, in blue line, while the open loop is in dotted line.

4.3.2 Choice of α_k with a modal constraint

The same example is repeated, but now the arbitrary parameters $\boldsymbol{\alpha}_k$ are determined by imposing a modal ratio constraints as explained in section 3.1.1. A value of $\rho = 1$ is chosen because this pole corresponds to a bending mode, so the movement of the 2 points on the wing registered by the laser sensors should be more or less the same. Thus, from (3.23), the system of equations to solve is

$$(\mathbf{e}_1^T - \mathbf{e}_2^T)\mathbf{R}_1\boldsymbol{\alpha}_1 = \mathbf{0} \qquad (\mathbf{e}_1^T - \mathbf{e}_2^T)\mathbf{R}_2\boldsymbol{\alpha}_2 = \mathbf{0}$$

obtaining

$$\alpha_{\mu_1,1} = \frac{r_{\mu_1,(2,2)} - r_{\mu_1,(1,2)}}{r_{\mu_1,(1,1)} - r_{\mu_1,(2,1)}} = 0.36 - 0.17i \qquad \alpha_{\mu_1,2} = 1$$

$$\alpha_{\mu_2,1} = \frac{r_{\mu_2,(2,2)} - r_{\mu_2,(1,2)}}{r_{\mu_2,(1,1)} - r_{\mu_2,(2,1)}} = 0.36 + 0.17i \qquad \alpha_{\mu_2,2} = 1$$

With these values, the eigenvectors corresponding to the assigned poles, calculated by the equation (3.11), are proportional to $\mathbf{w}_{1,2} = [1 \quad 1]^T$, as expected by the modal constraint imposition. Thus, the modal shape in closed loop is kept similar as the open loop one. With the receptance method

$$\mathbf{F} = \begin{bmatrix} -26.6 & -63.9 \\ -14.4 & -37.7 \end{bmatrix} \qquad \mathbf{G} = \begin{bmatrix} -120.0 & 233.9 \\ -186.5 & -158.4 \end{bmatrix}$$

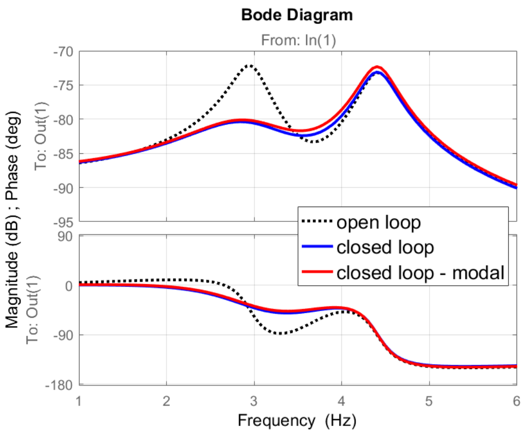

(a) 1^{st} output excited by 1^{st} input

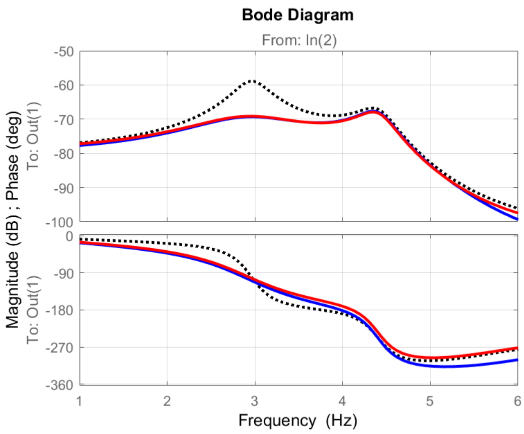

(b) 1^{st} output excited by 2^{nd} input

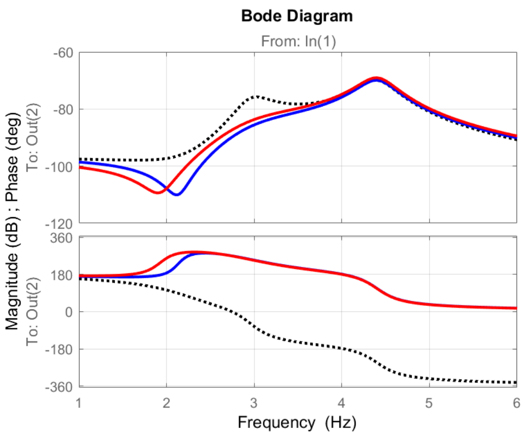

(c) 2^{nd} output excited by 1^{st} input

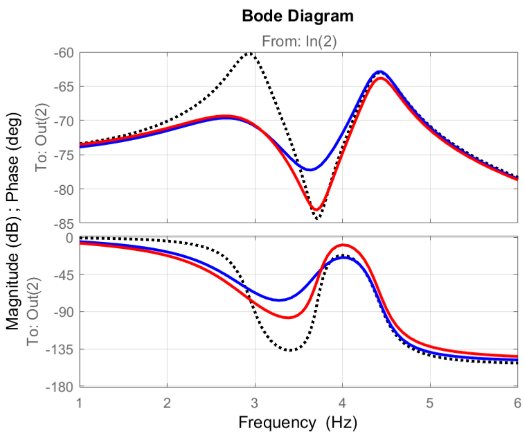

(d) 2^{nd} output excited by 2^{nd} input

Figure 4.8: Bode diagrams of the wing numerical model. Dotted line represents the open loop, blue line is the closed loop with only a simple pole damping increase, red line is the same, but with a modal constraint

The gain matrices show lower values as expected. Indeed, the control force necessary to move the poles is now lower, because it needs to move only the eigenvalues and not also the eigenvectors.

Bode diagrams of the system in closed loop with the latest gains are shown in Figure 4.8, in red line. There are not significant differences by comparing them with the ones obtained without constraint, but, in this case, the new chosen eigenvectors are not casual.

Pole-zero map of the open loop and the closed loop obtained with the modal constraint is shown in Figure 4.9. Also in this situation, all the other not shown poles are stable.

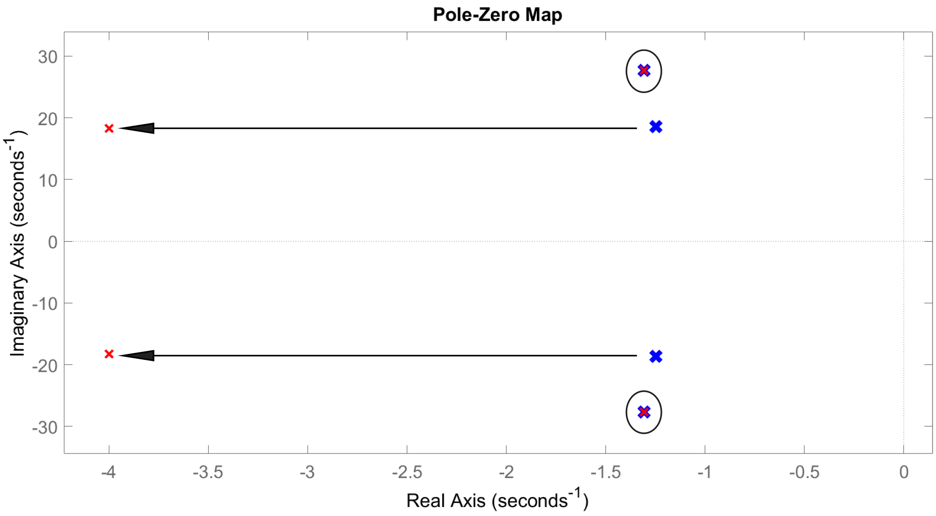

Figure 4.9: Pole-zero map of the wing numerical model. Blue X are the poles in open loop, while red X are the poles in closed loop with only one pole damping increase and a modal constraint

4.4 Example of 2 system poles placement with damping increment

Both the analysed modes are double in their damping now. Therefore, the assigned poles are

$$\mu_{1,2} = -2.5 \pm 18.43i \qquad \mu_{3,4} = -2.6 \pm 27.58i$$

The arbitrary parameters are chosen now with a ratio constraint $\rho_1 = 1$ for the poles of the first bending mode ($\mu_{1,2}$) and $\rho_2 = -0.5$ for the poles of the first torsional one ($\mu_{3,4}$), so to have $\mathbf{w}_{1,2} = [1 \quad 1]^T$ and $\mathbf{w}_{3,4} = [1 \quad -2]^T$. This is done to keep the closed loop eigenvectors close enough to the natural eigenvectors, and thus to reduce the control force needed to move the poles. So, $\boldsymbol{\alpha}_k$ are calculated by solving

$$(\mathbf{e}_1^T - \mathbf{e}_2^T)\mathbf{R}_1\boldsymbol{\alpha}_1 = \mathbf{0} \qquad (\mathbf{e}_1^T - \mathbf{e}_2^T)\mathbf{R}_2\boldsymbol{\alpha}_2 = \mathbf{0}$$

$$(\mathbf{e}_1^T + 0.5\mathbf{e}_2^T)\mathbf{R}_3\boldsymbol{\alpha}_3 = \mathbf{0} \qquad (\mathbf{e}_1^T + 0.5\mathbf{e}_2^T)\mathbf{R}_4\boldsymbol{\alpha}_4 = \mathbf{0}$$

In this way, the arbitrary parameters are

$$\alpha_{\mu_1,1} = \frac{r_{\mu_1,(2,2)} - r_{\mu_1,(1,2)}}{r_{\mu_1,(1,1)} - r_{\mu_1,(2,1)}} = -0.86 - 0.27i \qquad \alpha_{\mu_1,2} = 1$$

$$\alpha_{\mu_2,1} = \frac{r_{\mu_2,(2,2)} - r_{\mu_2,(1,2)}}{r_{\mu_2,(1,1)} - r_{\mu_2,(2,1)}} = -0.86 + 0.27i \qquad \alpha_{\mu_2,2} = 1$$

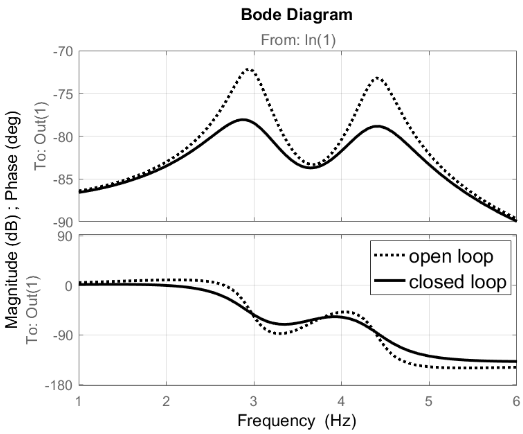

(a) 1^{st} output excited by 1^{st} input

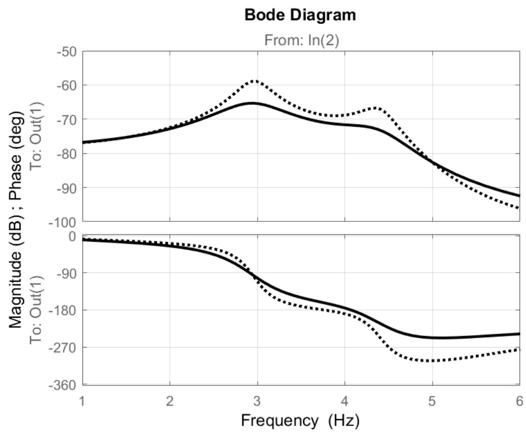

(b) 1^{st} output excited by 2^{nd} input

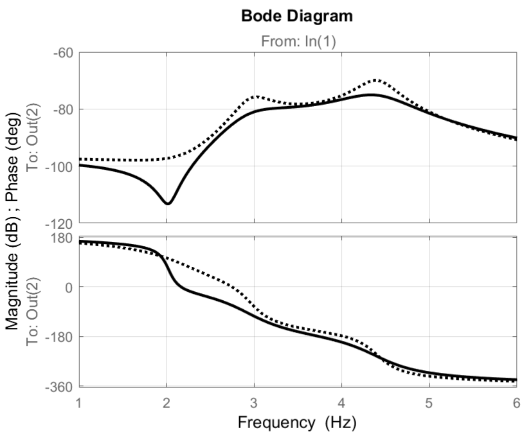

(c) 2^{nd} output excited by 1^{st} input

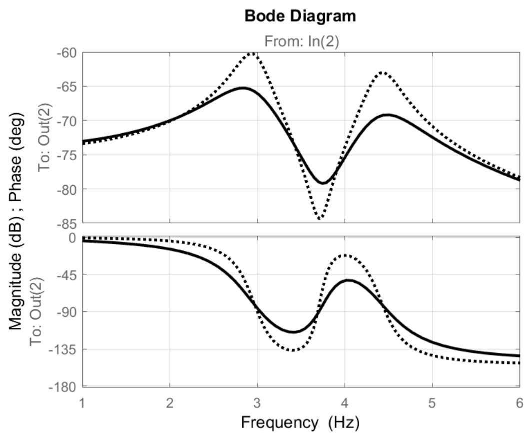

(d) 2^{nd} output excited by 2^{nd} input

Figure 4.10: Bode diagrams of the wing numerical model. Dotted line represents the open loop, solid line is the closed loop with a damping increment for both poles

$$\alpha_{\mu_3,1} = \frac{-0.5 r_{\mu_3,(2,2)} - r_{\mu_3,(1,2)}}{r_{\mu_3,(1,1)} + 0.5 r_{\mu_3,(2,1)}} = 12.94 - 2.83i \qquad \alpha_{\mu_3,2} = 1$$

$$\alpha_{\mu_4,1} = \frac{-0.5 r_{\mu_4,(2,2)} - r_{\mu_4,(1,2)}}{r_{\mu_4,(1,1)} + 0.5 r_{\mu_4,(2,1)}} = 12.94 + 2.83i \qquad \alpha_{\mu_4,2} = 1$$

With the application of the receptance method, the feedback gains are

$$\mathbf{F} = \begin{bmatrix} -56.5 & -39.0 \\ 93.3 & -10.4 \end{bmatrix} \qquad \mathbf{G} = \begin{bmatrix} -736.4 & 185.3 \\ 244.3 & 84.2 \end{bmatrix}$$

which are used for the closed loop control, and modify the system as shown in Bode diagrams of Figure 4.10.

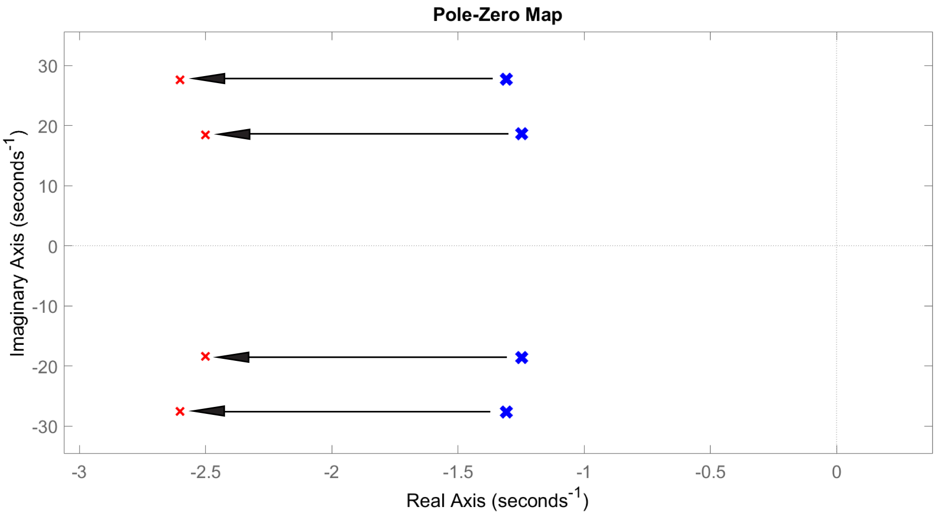

Figure 4.11: Pole-zero map of the wing numerical model. Blue X are the poles in open loop, while red X are the poles in closed loop with a damping increment of both poles

The pole-zero map of the system in open and closed loop is shown in Figure 4.11, zoomed on the 2 placed poles. Also in this case, the closed loop system remains stable in closed loop.

The receptance method is so proved on the numerical model of the MODFLEX wing, leading to a shift of its poles in every desired position. Its application results very simple and fast, and its implementation to a system with more inputs or outputs is possible without modifications of the algorithm.

Chapter 5

Control analysis of the wing experimental model

The receptance method was applied on the experimental wing and this chapter contains the results that have been obtained. The MODFLEX wing was setted up as explained in section 2.1.2. The receptance method was then applied with the following steps:

- The wing was fixed inside the test section, by placing it in the wind tunnel at a specific air speed.
- Open loop FRFs were computed by using the Siemens.PLM LMS Test.Lab acquisition system. The frequency range of interest comprised the first 2 system modes. The control surfaces were used as input one at time, with a stepped sine excitation at a fixed amplitude, by measuring their angular displacement with the digital encoder. Laser sensors readings were used as output.
- The open loop frequencies and damping values were computed from the FRFs by the modal parameter estimation technique PolyMAX.
- A state-space formulation was computed from the measured FRFs by using the SDTools MATLAB Toolbox.
- Closed loop poles for the first bending and first torsional modes were chosen, with also a modal constraint that determined the closed loop eigenvectors.
- The transfer function matrix of the state-space system was used with the MATLAB algorithm of the receptance method, as described in section 3.2, to compute displacement and velocity gains.
- **F** and **G** gains were included inside the Simulink control algorithm of the wing, implemented with the dSPACE real-time acquisition system.
- Closed loop FRFs were computed as done for the open loop ones.
- The closed loop frequencies and damping were computed by PolyMAX and compared with the open loop values. Also the flutter speed was compared.

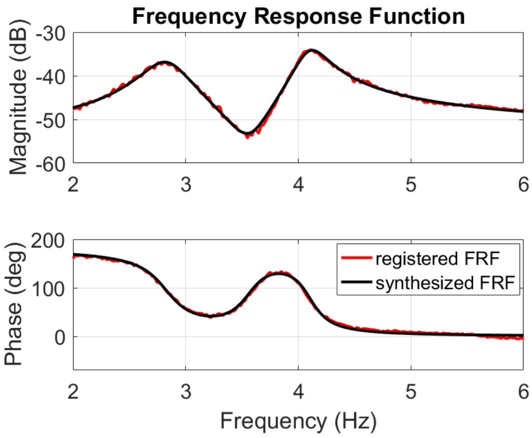

(a) LS1 output from LEO input

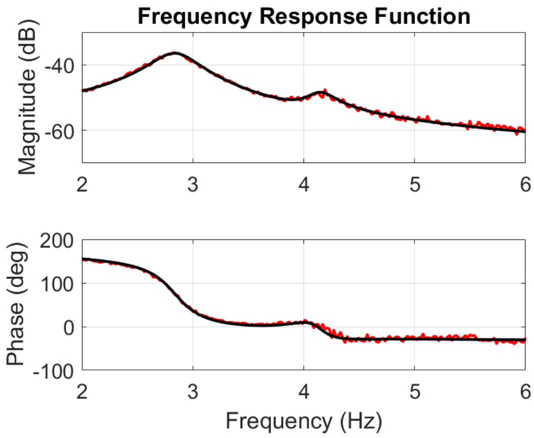

(b) LS1 output from TEO input

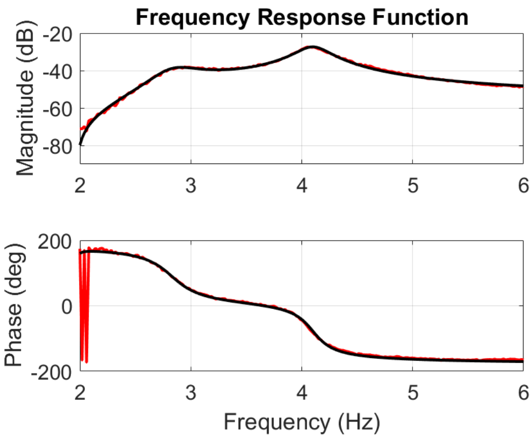

(c) LS2 output from LEO input

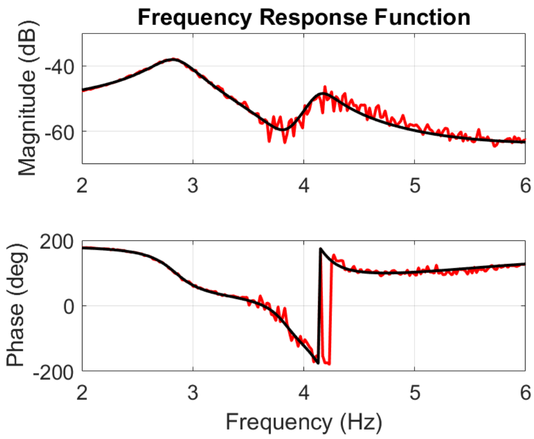

(d) LS2 output from TEO input

Figure 5.1: Open loop frequency response functions of the wing experimental model with a wind speed of 10 m/s. Red line represents the registered response, black line is the synthesized curve

5.1 Open loop system with a wind speed of 10 m/s

The MODFLEX wing was mounted inside its test section and positioned in the low-speed wind tunnel of the University of Liverpool, with a wind speed of 10 m/s. Then, open loop FRFs were computed with LMS Test.Lab, actuating one control surface at time with a stepped sine excitation, and keeping the other one fixed. The range of frequency for the input was between 2 and 6 Hz, with an increment of 0.02 Hz and 10 cycles at each frequency. An excitation amplitude of 2 degrees was selected both for the LEO and the TEO control surface.

Frequency and damping values of each peak were computed by the modal parameter

Table 5.1: Closed loop control tests performed on the wing experimental model

Test	Tested control	new poles $\mu_{1,2}$	new poles $\mu_{3,4}$
1	$\times 2$ damping 2^{nd} mode	-	$-1.78 \pm 25.78i$
2	$\times 3$ damping 2^{nd} mode	-	$-2.67 \pm 25.71i$
3	$\times 2$ damping 1^{st} and 2^{nd} mode	$-2.51 \pm 17.65i$	$-1.78 \pm 25.78i$
4	$\times 1.2$ frequency 2^{nd} mode	-	$-1.07 \pm 30.99i$
5	$\times 0.9$ freq. 1^{st} mode, $\times 1.1$ freq. 2^{nd} mode	$-1.13 \pm 16.00i$	$-0.98 \pm 28.41i$

estimation technique PolyMAX, and shown in Table 5.2. In this way, it was possible to synthesize the curves by eliminating all the noise obtained with the responses. Both the registered responses and the synthesized curves are in Figure 5.1, which correspond to the laser sensor readings LS1 and LS2 with LEO and TEO control surface commands.

The state-space formulation of the experimental wing was computed with SDTools. Naturally, it is a state-space system with 2 inputs and 2 outputs. Moreover, this system has 4 states, and from the $\mathbf{A_{ss}}$ matrix it was possible to find the 4 system eigenvalues, which corresponded to the bending and torsional modes. They are

$$\lambda_{1,2} = -1.255 \pm 17.780i \qquad \lambda_{3,4} = -0.889 \pm 25.829i$$

These values can also be found from the natural frequency and damping values obtained by PolyMAX. Prior to the application of the receptance method, the state-space system was multiplied by the transfer function of the laser sensors filter, not considered with the computation of the open loop FRFs.

5.2 Closed loop control with the receptance method

The transfer function matrix, computed from the open loop state-space system, is directly linked with the receptance matrix. This measured receptance was used inside the MATLAB algorithm, described in the previous chapters, to find **F** and **G** gains. Different closed loop controls were tested, placing new poles in various positions. All the investigated options are presented in Table 5.1.

5.2.1 Test 1 - Double damping for the 2^{nd} mode

As first test, only the second mode was moved, retaining $\lambda_{1,2}$. With a double value for the damping, the second poles couple is

$$\mu_{3,4} = -1.778 \pm 25.783i$$

Table 5.2: Open loop and all closed loops comparison for the experimental wing at 10 m/s of wind speed. Resonance frequencies, damping and flutter speed are compared. The difference between the registered and the expected values of frequency and damping for each closed loop test are in brackets

	1^{st} bending mode		1^{st} torsional mode		
	Freq. [Hz]	Damp. ζ [%]	Freq. [Hz]	Damp. ζ [%]	Flutter [m/s]
Open loop	2.84	7.04	4.11	3.44	13.5
CL Test 1	2.84 (0.0%)	7.98 (13.4%)	4.04 (1.7%)	7.01 (1.9%)	15.5
CL Test 2	2.82 (0.7%)	7.74 (9.9%)	4.08 (0.7%)	10.55 (2.2%)	16.5
CL Test 3	2.84 (0.0%)	13.06 (7.2%)	4.01 (2.4%)	6.81 (1.0%)	15.5
CL Test 4	2.84 (0.0%)	9.37 (33.1%)	4.99 (1.0%)	5.73 (66.6%)	14.0
CL Test 5	2.56 (0.4%)	7.84 (11.4%)	4.49 (0.7%)	4.82 (40.1%)	15.0

The arbitrary parameters $\boldsymbol{\alpha}_k$ were computed selecting a ratio constraint $\rho = -0.5$, so to have the new eigenvectors for this mode proportional to

$$\mathbf{w}_{3,4} = \begin{pmatrix} 1 \\ -2 \end{pmatrix}$$

which is similar to the natural eigenvector. Hence, the arbitrary parameters are obtained by

$$\alpha_{\mu_3,1} = \frac{-0.5 r_{\mu_3,(2,2)} - r_{\mu_3,(1,2)}}{r_{\mu_3,(1,1)} + 0.5 r_{\mu_3,(2,1)}} = 0.183 + 0.815i \qquad \alpha_{\mu_3,2} = 1$$

$$\alpha_{\mu_4,1} = \frac{-0.5 r_{\mu_4,(2,2)} - r_{\mu_4,(1,2)}}{r_{\mu_4,(1,1)} + 0.5 r_{\mu_4,(2,1)}} = 0.183 - 0.815i \qquad \alpha_{\mu_4,2} = 1$$

In this way, applying the receptance method, the feedback gains that lead to the desired pole placement are

$$\mathbf{F} = \begin{bmatrix} 0.373 & 0.584 \\ -0.608 & -0.387 \end{bmatrix} \qquad \mathbf{G} = \begin{bmatrix} -7.538 & 11.349 \\ 5.216 & -16.731 \end{bmatrix}$$

These feedback gains were included to the Simulink control model and then closed loop FRFs were computed in the same manners as done for the open loop ones, with a wind speed of 10 m/s. The same frequency range and step, and also the same amplitudes for the control surfaces were selected. Synthesized closed loop FRFs are in Figure 5.2, compared with the open loop ones. The closed loop frequencies and damping values were computed with the PolyMAX technique. Results are in Table 5.2, with also the percent difference between them and the expected results. A good response was obtained in this case, as shown by the percentage.

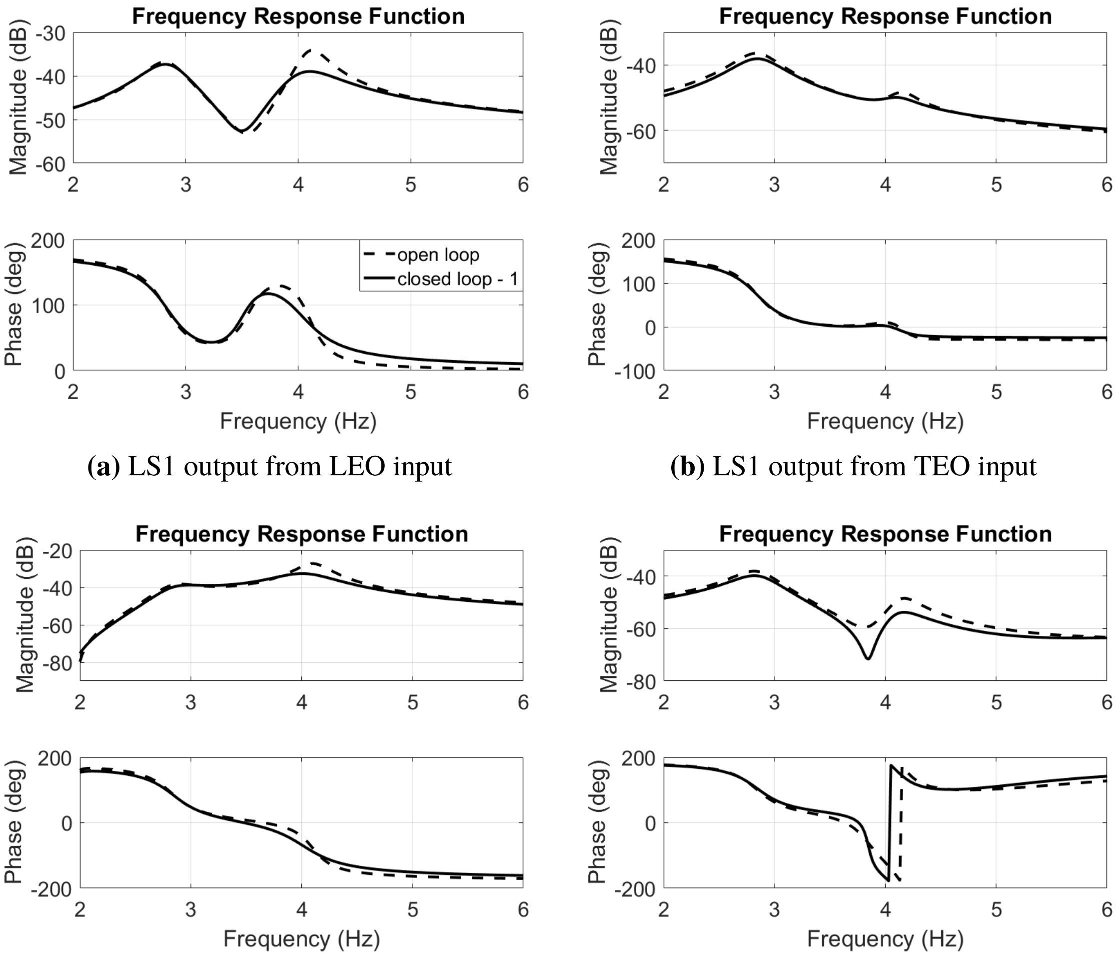

(a) LS1 output from LEO input

(b) LS1 output from TEO input

(c) LS2 output from LEO input

(d) LS2 output from TEO input

Figure 5.2: Synthesized frequency response functions of the 1^{st} closed loop test performed on the experimental wing. They are computed with a wind speed of 10 m/s and compared with the open loop FRFs

The flutter point was determined by increasing the wind speed with steps of 0.5 m/s until the instability, obtaining it at 15.5 m/s. This result is also in Table 5.2. Compared with the open loop flutter speed, and increase of 15% is obtained by this closed loop test, an expected result because the torsional mode damping is the one leading to flutter.

5.2.2 Test 2 - Triple damping for the 2$^{\text{nd}}$ mode

The second mode damping was multiplied by 3 as second test, keeping again the first mode unchanged. Thus, assigned poles are

$$\mu_{3,4} = -2.667 \pm 25.706i$$

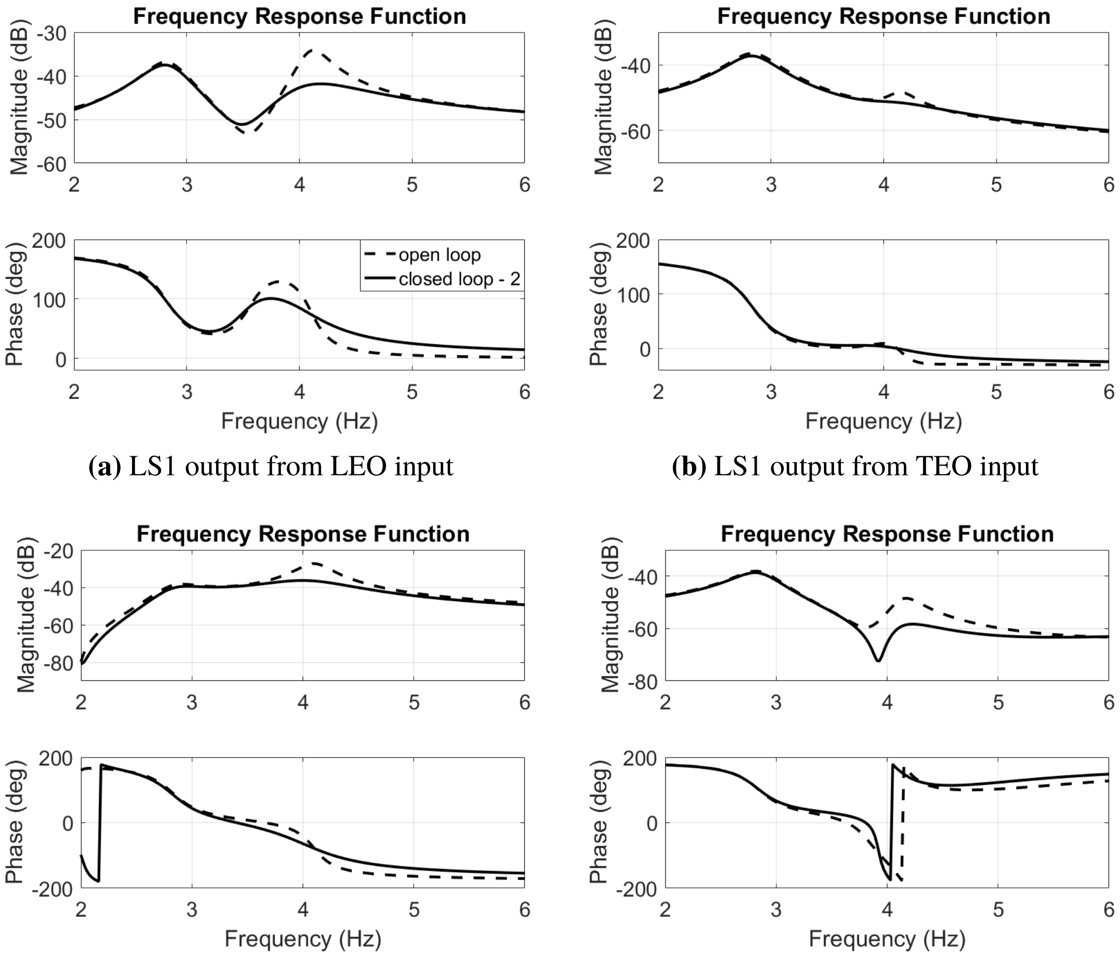

(a) LS1 output from LEO input

(b) LS1 output from TEO input

(c) LS2 output from LEO input

(d) LS2 output from TEO input

Figure 5.3: Synthesized frequency response functions of the 2^{nd} closed loop test on the experimental wing. They are computed with a wind speed of 10 m/s and compared with the open loop FRFs

The arbitrary parameters were computed in the same way, so they are

$$\alpha_{\mu_3,1} = -0.624 + 1.003i \qquad \alpha_{\mu_3,2} = 1$$

$$\alpha_{\mu_4,1} = -0.624 - 1.003i \qquad \alpha_{\mu_4,2} = 1$$

The new gains obtained by the receptance method, and used to perform this closed loop test, are

$$\mathbf{F} = \begin{bmatrix} 0.781 & 0.185 \\ -1.177 & 0.324 \end{bmatrix} \qquad \mathbf{G} = \begin{bmatrix} -11.857 & 21.861 \\ 6.699 & -24.939 \end{bmatrix}$$

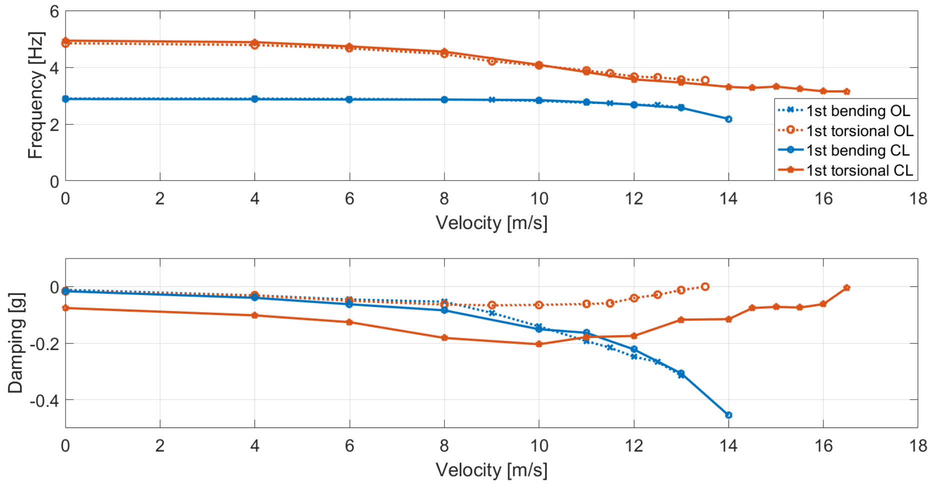

Figure 5.4: Velocity-frequency and Velocity-damping diagrams of the MODFLEX wing in closed loop with a triple damping value of the 1^{st} torsional mode, compared with the open loop results

Synthesized FRFs in closed loop are in Figure 5.3, compared with the open loop responses. Frequency and damping results are also in Table 5.2, showing a good correlation with the expectations.

Flutter test

A flutter test, as done in section 2.3.2, was performed with this closed loop control test. The experimental V-f and V-g plots are shown in Figure 5.4, compared with the open loop results. The flutter point is registered to happen at a speed of 16.5 m/s. An increase of 22% is so obtained by tripling the torsional mode damping value, and it is a really important result. In figure, the bending mode in closed loop is plotted until 14 m/s because the high value of damping made it difficult to find the peak from the frequency response functions.

5.2.3 Test 3 - Double damping for the first 2 modes

The damping of both the first 2 wing modes were doubled in this test, to see if also an increase of the first bending mode damping is related with the flutter point of the MODFLEX wing. For this test, the new desired poles are

$$\mu_{1,2} = -2.510 \pm 17.647i \qquad \mu_{3,4} = -1.778 \pm 25.783i$$

In order to keep the placed eigenvectors near to the natural ones, the arbitrary parameters were calculated by imposing a ratio constraint $\rho_1 = 1$ for the first bending mode and

$\rho_2 = -0.5$ for the first torsional mode, so to have

$$\mathbf{w}_{1,2} = \begin{pmatrix} 1 \\ 1 \end{pmatrix} \qquad \mathbf{w}_{3,4} = \begin{pmatrix} 1 \\ -2 \end{pmatrix}$$

The arbitrary parameters to use are

$$\alpha_{\mu_1,1} = \frac{r_{\mu_1,(2,2)} - r_{\mu_1,(1,2)}}{r_{\mu_1,(1,1)} - r_{\mu_1,(2,1)}} = -0.460 + 0.087i \qquad \alpha_{\mu_1,2} = 1$$

$$\alpha_{\mu_2,1} = \frac{r_{\mu_2,(2,2)} - r_{\mu_2,(1,2)}}{r_{\mu_2,(1,1)} - r_{\mu_2,(2,1)}} = -0.460 - 0.087i \qquad \alpha_{\mu_2,2} = 1$$

$$\alpha_{\mu_3,1} = \frac{-0.5r_{\mu_3,(2,2)} - r_{\mu_3,(1,2)}}{r_{\mu_3,(1,1)} + 0.5r_{\mu_3,(2,1)}} = 0.183 + 0.815i \qquad \alpha_{\mu_3,2} = 1$$

$$\alpha_{\mu_4,1} = \frac{-0.5r_{\mu_4,(2,2)} - r_{\mu_4,(1,2)}}{r_{\mu_4,(1,1)} + 0.5r_{\mu_4,(2,1)}} = 0.183 - 0.815i \qquad \alpha_{\mu_4,2} = 1$$

The receptance method algorithm gives the gains

$$\mathbf{F} = \begin{bmatrix} -1.179 & 3.677 \\ -1.384 & 1.160 \end{bmatrix} \qquad \mathbf{G} = \begin{bmatrix} 5.874 & -22.787 \\ 11.922 & -33.798 \end{bmatrix}$$

which were used to compute the closed loop FRFs, shown in Figure 5.5. Frequencies and damping are in Table 5.2. Also in this case, good results were achieved, obtaining frequencies and damping similar to the expected values. However, a spillover problem happened, with a vibration at high frequency for the trailing edge control surface when the first bending peak was reached. This problem could be solved in future by considering also other modes over the first two, in order to retain also high frequency poles.

The flutter point was registered to be at 15.5 m/s, as obtained with the test 1. Thus, an increment of the first bending damping does not affect the flutter speed, because the flutter instability is caused by the first torsional damping that becomes zero.

5.2.4 Test 4 - Frequency increase for the 2^nd mode

An increase of damping was just proved with the single-input control by Fichera et al. [24], while a movement of frequency was never tested on the MODFLEX wing. In this section it is described the frequency shift on the torsional mode test. Thus, desired poles of the closed loop are

$$\mu_{3,4} = -1.067 \pm 30.994i$$

while $\lambda_{1,2}$ are kept unchanged. The same modal constraint selected for the other tests was chosen, so with a ratio $\rho = -0.5$. The arbitrary parameters obtained in the same manner are

$$\alpha_{\mu_3,1} = -0.564 + 0.005i \qquad \alpha_{\mu_3,2} = 1$$

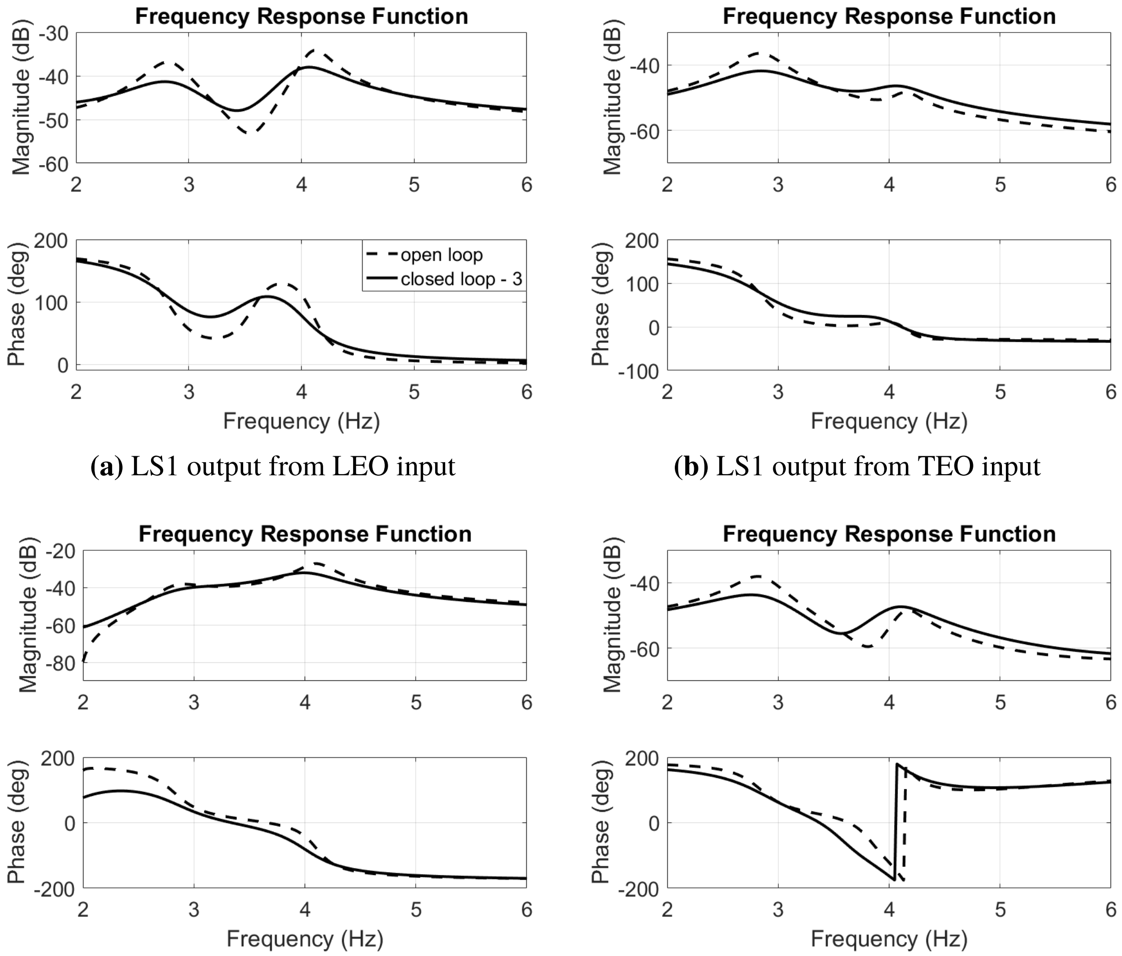

(a) LS1 output from LEO input

(b) LS1 output from TEO input

(c) LS2 output from LEO input

(d) LS2 output from TEO input

Figure 5.5: Synthesized frequency response functions of the 3^{rd} closed loop test on the experimental wing. They are computed with a wind speed of 10 m/s and compared with the open loop FRFs

$$\alpha_{\mu_4,1} = -0.564 - 0.005i \qquad \alpha_{\mu_4,2} = 1$$

The feedback gains calculated with the receptance method are

$$\mathbf{F} = \begin{bmatrix} 1.690 & -3.026 \\ -0.330 & 0.630 \end{bmatrix} \qquad \mathbf{G} = \begin{bmatrix} 65.199 & -115.159 \\ -83.207 & 147.287 \end{bmatrix}$$

With these values, the closed loop FRFs were computed. The synthesized graphs are in Figure 5.6, compared with the open loop ones. Modal results are in Table 5.2, which show a great difference for both the damping values compared with the expectations. It is uncertain if it is due to an error of the wind speed or if the frequency shift modify also the damping values.

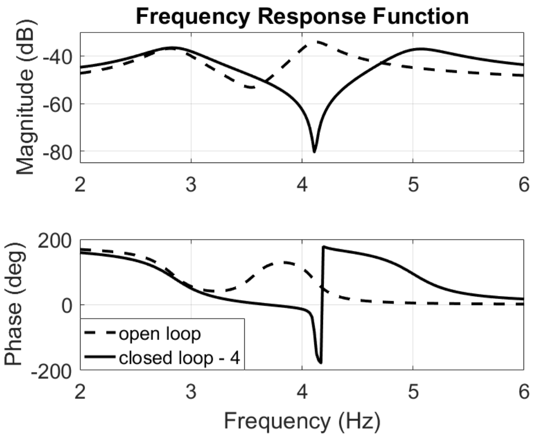

(a) LS1 output from LEO input

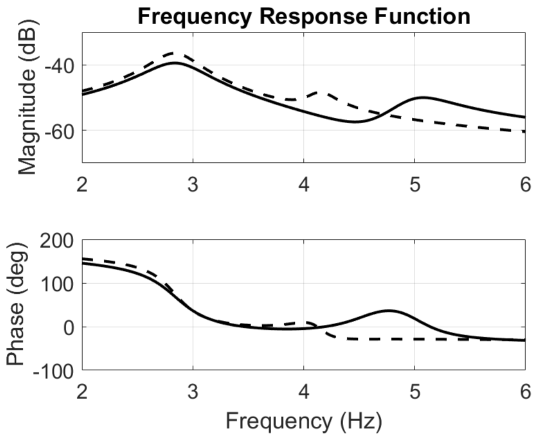

(b) LS1 output from TEO input

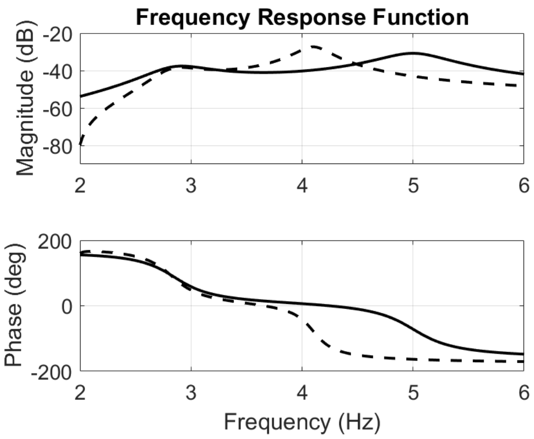

(c) LS2 output from LEO input

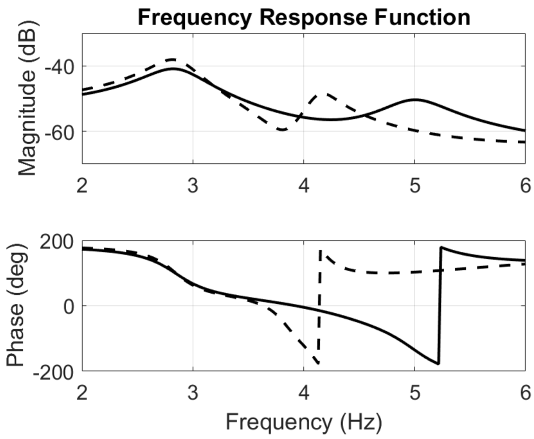

(d) LS2 output from TEO input

Figure 5.6: Synthesized frequency response functions of the 4^{th} closed loop test on the experimental wing. They are computed with a wind speed of 10 m/s and compared with the open loop FRFs

An increase of the wind speed revealed that the flutter point was not moved significantly, so a frequency increase is not a good way to increase the flutter boundary of the MODFLEX wing. However, the receptance method was proved also for a natural frequency movement.

5.2.5 Test 5 - Frequency shift for the first 2 modes

As last test, the frequency of both the first bending and the first torsional mode were moved, by increasing the distance between them. One was multiplied by 0.9, the other was multiplied by 1.1. New poles were calculated, obtaining

$$\mu_{1,2} = -1.129 \pm 16.002i \qquad \mu_{3,4} = -0.978 \pm 28.412i$$

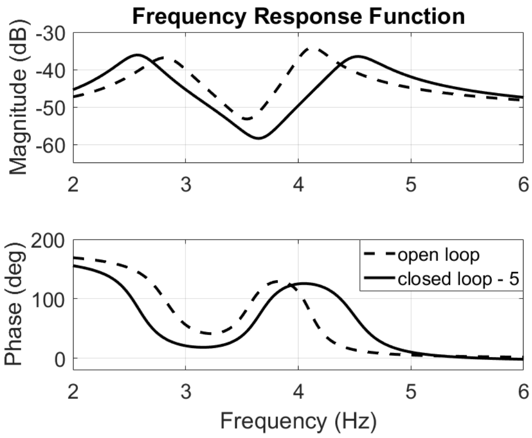

(a) LS1 output from LEO input

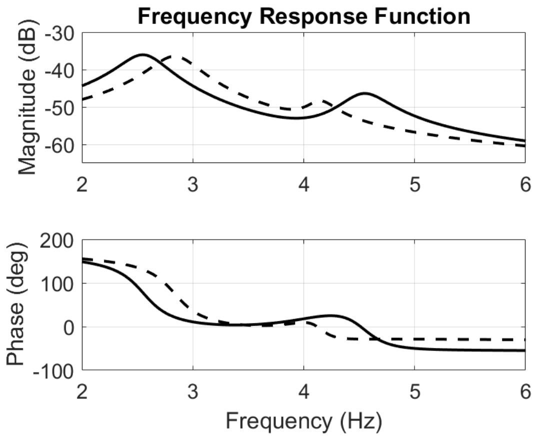

(b) LS1 output from TEO input

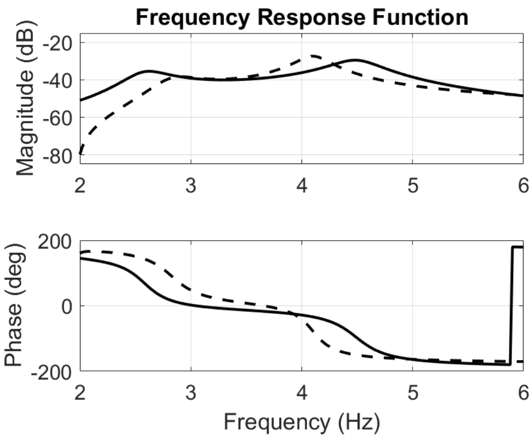

(c) LS2 output from LEO input

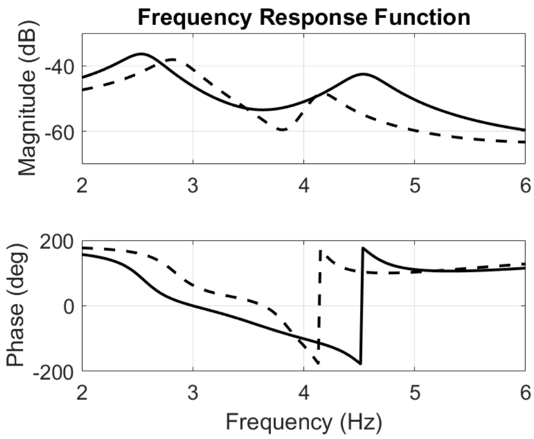

(d) LS2 output from TEO input

Figure 5.7: Synthesized frequency response functions of the 5^{th} closed loop test on the experimental wing. They are computed with a wind speed of 10 m/s and compared with the open loop FRFs

With the same modal constraints, the arbitrary parameters are

$$\begin{aligned}
\alpha_{\mu_1,1} &= -0.289 + 0.542i & \alpha_{\mu_1,2} &= 1 \\
\alpha_{\mu_2,1} &= -0.289 - 0.542i & \alpha_{\mu_2,2} &= 1 \\
\alpha_{\mu_3,1} &= -0.652 - 0.230i & \alpha_{\mu_3,2} &= 1 \\
\alpha_{\mu_4,1} &= -0.652 + 0.230i & \alpha_{\mu_4,2} &= 1
\end{aligned}$$

and the obtained feedback gains are

$$\mathbf{F} = \begin{bmatrix} -2.258 & 0.358 \\ -1.751 & 0.111 \end{bmatrix} \qquad \mathbf{G} = \begin{bmatrix} 52.774 & -130.678 \\ -28.262 & 16.801 \end{bmatrix}$$

The closed loop FRFs are presented in Figure 5.7, compared with the open loop. In Table 5.2 there are the frequency and damping values, computed with PolyMAX. Also in this test, an increase of the damping value for the second mode was registered, so it is probable that a change on the natural frequencies modifies also the damping behaviour with the wind speed.

The flutter point, in this case, increased to 15 m/s, as shown in the same table. This result explains that also a movement of the frequencies, by increasing the distance between them, is a solution for flutter.

Chapter 6

Conclusions

The receptance method is proved to be a suitable way to extend the flight speed envelope of an aircraft, by shifting the flutter point at higher speed values. The flutter speed is increased via a partial pole placement by moving natural poles of the system to new desired positions with an active control. To do so, measured receptance data are the only information needed from the system, obtained from a modal test. Hence, there is no need to evaluate the structural matrices **M**, **C** and **K**, which is a very difficult work for complex systems.

The method was used in its last reformulation, with a Multiple-Input Multiple-Output control approach. An advantage of the new reformulation is that it is possible to assign both the eigenvalues and the eigenvectors of the system. In this way, keeping the new eigenvectors close to the natural ones, smaller feedback gain values are obtained, which are more practically feasible.

The receptance method worked on the numerical model of a wing. Then, it was tested, with positive results, on the experimental flexible wing called MODFLEX. Different test were done on the wing, moving 1 or 2 couples of poles in different ways. The flutter point moved at higher speed for all of them, with a speed increase up to 22%. About the numerical model, it is validated since it fits well enough with the experimental results, registered by a modal and a flutter test.

Further developments of the experimental wing see it controlled with all the designed control surfaces, so with also the Leading Edge Inner and the Trailing Edge Inner (LEI and TEI) surfaces on the 2^{nd} sector. Furthermore, the receptance method can be applied on a different system, not only a wing, to be proved as general active control way useful to increase the flutter boundary.

Bibliography

[1] D.H. Hodges and G.A. Pierce, *Introduction to Structural Dynamics and Aeroelasticity*, Cambridge University Press, 2002

[2] K.Y. Billah and R.H. Scanlan, *Resonance, Tacoma Narrows bridge failure, and undergraduate physics textbooks*, American Journal of Physics 59 (2), 1990

[3] F.W. Lanchester, *Torsional Vibration of the Tail of an Aeroplane*, Aeronautical Research Committee Reports & Memoranda 276 (1), 1916

[4] L. Bairstow and A. Fage, *Oscillations of the Tail Plane and Body of an Aeroplane in Flight*, Aeronautical Research Committee Reports & Memoranda 276 (2), 1916

[5] Y.C. Fung, *An Introduction to the Theory of Aeroelasticity*, John Wiley & Sons, 1955

[6] R.L. Bisplinghoff, H. Ashley and R.L.Halfman, *Aeroelasticity*, Addison Wesley Publishing Company, 1955

[7] E.H. Dowell, H.C. Curtiss, R.H. Scanlan and F. Sisto, *A Modern Course in Aeroelasticity*, Sijthoff & Noordhoff International Publishers, 1978

[8] J.R. Wright and J.E. Cooper, *Introduction to Aircraft Aeroelasticity and Loads*, John Wiley & Sons, 2007

[9] J.E. Mottershead and Y.M. Ram, *Inverse eigenvalue problems in vibration absorption: Passive modification and active control*, Mechanical Systems and Signal Processing 20, p.5–44, 2006

[10] W.J. Duncan, *The admittance method for obtaining the natural frequencies of systems*, Philosophical Magazine 32, p.401-409, 1941

[11] W.M. Wonham, *On pole assignment in multi-input controllable linear systems*, IEEE Transactions on Automatic Control 12 (6), p.660-665, 1967

[12] D.J. Inman, *Vibration with Control, Measurement and Stability*, Pearson College Div, 1989

[13] C.R. Fuller, S.J. Elliott and P.A. Nelson, *Active Control of Vibration*, Academic Press, 1997

[14] B.N. Datta, S. Elhay and Y.M. Ram, *Orthogonality and partial pole assignment for the symmetric definite quadratic pencil*, Linear Algebra and its Applications 257, p.29-48, 1997

[15] Z-J. Bai, B.N. Datta and J. Wang, *Robust and minimum norm partial quadratic eigenvalue assignment in vibrating systems: A new optimization approach*, Mechanical Systems and Signal Processing 24 (3), p.766-783, 2010

[16] Y.M. Ram and J.E. Mottershead, *Receptance method in active vibration control*, The American Institute of Aeronautics and Astronautics Journal 45 (3), p.562-567, 2007

[17] J.E. Mottershead, M.G. Tehrani and Y.M. Ram, *Assignment of eigenvalue sensitivities from receptance measurements*, Mechanical Systems and Signal Processing 23 (6), p.1931-1939, 2009

[18] Y.M. Ram, A. Singh and J.E. Mottershead, *State feedback control with time delay*, Mechanical Systems and Signal Processing 23, p.1940-1945, 2009

[19] J.E. Mottershead, M.G. Tehrani, S. James and Y.M. Ram, *Active vibration suppression by pole-zero placement using measured receptances*, Journal of Sound and Vibration 311 (3-5), p.1391-1408, 2008

[20] M.G. Tehrani, R.N.R. Elliott and J.E. Mottershead, *Partial pole placement in structures by the method of receptances: Theory and experiments*, Journal of Sound and Vibration 329, p.5017-5035, 2010

[21] J.E. Mottershead, M.G. Tehrani, S. James and P. Court, *Active vibration control experiments on an Agusta Westland W30 helicopter airframe*, Proceedings of the Institution of Mechanical Engineers, Part C: Journal of Mechanical Engineering Science 226 (6), p.1504-1516, 2012

[22] Y.M. Ram and J.E. Mottershead, *Multiple-input active vibration control by partial pole placement using the method of receptances*, Mechanical Systems and Signal Processing 40, p.727-735, 2013

[23] G.H. Golub and C.F. Van Loan, *Matrix Computations*, Johns Hopkins University Press, 1983

[24] S. Fichera, S. Jiffri and J.E. Mottershead, *Design and wind tunnel test of a MODular aeroelastic FLEXible wing (MODFLEX)*, The University of Liverpool Repository, 2016

[25] G.F. Franklin, J.D. Powell and A. Emami-Naeini, *Feedback Control of Dynamic Systems*, Pearson, 2010

[26] D.J. Ewins, *Modal Testing - theory, practice and application*, Research Studies Press LTD, 2000

[27] B. Peeters, G. Lowet, H. Van der Auweraer and J. Leuridan, *A New Procedure for Modal Parameter Estimation*, Sound and Vibration 38 (1), p.24-28, 2004